



**HAL**  
open science

## Combustion for aircraft propulsion: Progress in advanced laser-based diagnostics on high-pressure kerosene/air flames produced with low-NO<sub>x</sub> fuel injection systems

Sylvain Legros, Clément Brunet, Patricia Domingo-Alvarez, Pierre Malbois, Erwan Salaun, Gilles Godard, Marcos Caceres, Benoît Barviau, Gilles Cabot, Bruno Renou, et al.

### ► To cite this version:

Sylvain Legros, Clément Brunet, Patricia Domingo-Alvarez, Pierre Malbois, Erwan Salaun, et al.. Combustion for aircraft propulsion: Progress in advanced laser-based diagnostics on high-pressure kerosene/air flames produced with low-NO<sub>x</sub> fuel injection systems. *Combustion and Flame*, 2021, 224, pp.273-294. 10.1016/j.combustflame.2020.12.036 . hal-03132265

**HAL Id: hal-03132265**

**<https://hal.science/hal-03132265v1>**

Submitted on 30 Nov 2021

**HAL** is a multi-disciplinary open access archive for the deposit and dissemination of scientific research documents, whether they are published or not. The documents may come from teaching and research institutions in France or abroad, or from public or private research centers.

L'archive ouverte pluridisciplinaire **HAL**, est destinée au dépôt et à la diffusion de documents scientifiques de niveau recherche, publiés ou non, émanant des établissements d'enseignement et de recherche français ou étrangers, des laboratoires publics ou privés.

# Combustion and Flame

## Combustion for aircraft propulsion: progress in advanced laser-based diagnostics on high-pressure kerosene/air flames produced with low-NOx fuel injection systems

--Manuscript Draft--

<b>Manuscript Number:</b>	CNF-D-20-01057
<b>Article Type:</b>	Special Issue for Ron Hanson
<b>Keywords:</b>	PIV, PDA, OH-PLIF, kerosene-PLIF, NO-PLIF, CPP fs-CARS, Turbulent swirled flame, High pressure, spray combustion, Lean premixed fuel injector, Kerosene fuel, Large Eddy Simulation,
<b>Abstract:</b>	<p>The challenges in designing high-performance aeronautical combustion systems have not changed significantly over the years, but the increase of stringent regulations and the need to tackle rising fuel prices require new sophisticated analysis processes. To address this concern, the first objective of the current study has consisted of performing experiments on an innovative lean premixed injection system designed for helicopter engines and fed with liquid kerosene (Jet A1) using various advanced laser-based diagnostics capable of performing measurements in high-pressure multi-phase flows. The employed laser diagnostics included the Particle Image Velocimetry (PIV), Phase Doppler Anemometry (PDA) and Planar laser-induced fluorescence (PLIF) of OH, kerosene vapor and NO. These diagnostics were used individually or in combination for custom-made solutions for accessing to detailed information on the spatial distributions of velocity, droplets size, OH, kerosene and NO molar fractions in pressure conditions ranging from 0.4 to 1.8 MPa. Additional measurements with the chirped probe pulse femtosecond coherent anti-Stokes Raman scattering (CPP fs-CARS) thermometry were also performed on similar high-pressure kerosene/air flames to demonstrate the ability to perform time-series of temperature measurements under realistic pressure conditions. Further, Large-Eddy simulations of the current flame were performed using the PCM-FPI tabulated chemistry approach. The two-phase flow was calculated by a polydisperse Euler-Lagrangian approach. In these simulations, the impact of the spray characteristics on the flame is analysed through a dedicated parametric study involving four inlet droplet size distributions. Numerical simulations allow to conclude on the importance of the size of the droplets injected into the flow. The droplet size distribution injected from the fuel nozzle will affect not only the aerodynamic field but also the flame structure and its anchorage point as well as the spatial distribution of the fuel and OH species. This is confirmed by the comparisons made between the numerical predictions and the numerous experimental data which show that only one inlet droplet size distribution allows to simulate the experimental results not on a single scalar parameter like commonly the flame structure but on all the measured scalar parameters for which comparisons with the numerical predictions are accessible.</p>

# Combustion for aircraft propulsion: progress in advanced laser-based diagnostics on high-pressure kerosene/air flames produced with low-NO<sub>x</sub> fuel injection systems

S. Legros<sup>1</sup>, C. Brunet<sup>1</sup>, P. Domingo-Alvarez<sup>1</sup>, P. Malbois<sup>1</sup>, E. Salaun<sup>1</sup>, G. Godard<sup>1</sup>, M. Caceres<sup>1</sup>, B. Barviau<sup>1</sup>, G. Cabot<sup>1</sup>, B. Renou<sup>1</sup>, G. Lartigue<sup>1</sup>, V. Moureau<sup>1</sup>, S. Puggelli<sup>2</sup>, S. Richard<sup>3</sup>, M. Boukhalfa<sup>1</sup> and F. Grisch<sup>1</sup>

<sup>1</sup> Normandie Univ., UNIROUEN, INSA Rouen, CNRS, CORIA, 76000 Rouen, France

<sup>2</sup> SAFRAN Tech, Paris-Saclay, France

<sup>3</sup> SAFRAN Helicopter Engines, Bordes, France

## Abstract:

The challenges in designing high-performance aeronautical combustion systems have not changed significantly over the years, but the increase of stringent regulations and the need to tackle rising fuel prices require new sophisticated analysis processes. To address this concern, the first objective of the current study has consisted of performing experiments on an innovative lean premixed injection system designed for helicopter engines and fed with liquid kerosene (Jet A1) using various advanced laser-based diagnostics capable of performing measurements in high-pressure multi-phase flows. The employed laser diagnostics included the Particle Image Velocimetry (PIV), Phase Doppler Anemometry (PDA) and Planar laser-induced fluorescence (PLIF) of OH, kerosene vapor and NO. These diagnostics were used individually or in combination for custom-made solutions for accessing to detailed information on the spatial distributions of velocity, droplets size, OH, kerosene and NO molar fractions in pressure conditions ranging from 0.4 to 1.8 MPa. Additional measurements with the chirped probe pulse femtosecond coherent anti-Stokes Raman scattering (CPP fs-CARS) thermometry were also performed on similar high-pressure kerosene/air flames to demonstrate the ability to perform time-series of temperature measurements under realistic pressure conditions. Further, Large-Eddy simulations of the current flame were performed using the PCM-FPI tabulated chemistry approach. The two-phase flow was calculated by a polydisperse Euler-Lagrangian approach. In these simulations, the impact of the spray characteristics on the flame is analysed through a dedicated parametric study involving four inlet droplet size distributions. Numerical simulations allow to conclude on the importance of the size of the droplets injected into the flow. The droplet size distribution injected from the fuel nozzle will affect not only the aerodynamic field but also the flame structure and its anchorage point as well as the spatial

1  
2  
3  
4  
5  
6  
7  
8  
9  
10  
11  
12  
13  
14  
15  
16  
17  
18  
19  
20  
21  
22  
23  
24  
25  
26  
27  
28  
29  
30  
31  
32  
33  
34  
35  
36  
37  
38  
39  
40  
41  
42  
43  
44  
45  
46  
47  
48  
49  
50  
51  
52  
53  
54  
55  
56  
57  
58  
59  
60  
61  
62  
63  
64  
65

distribution of the fuel and OH species. This is confirmed by the comparisons made between the numerical predictions and the numerous experimental data which show that only one inlet droplet size distribution allows to simulate the experimental results not on a single scalar parameter like commonly the flame structure but on all the measured scalar parameters for which comparisons with the numerical predictions are accessible.

**Keywords:** PIV, PDA, OH-PLIF, kerosene-PLIF, NO-PLIF, CPP fs-CARS, Turbulent swirled flame, High pressure, spray combustion, Lean premixed fuel injector, Kerosene fuel, Large Eddy Simulation,

**Corresponding author:** Prof. Frédéric Grisch

Mailing address: UMR 6614 CORIA, INSA de Rouen Normandie  
Site Universitaire du Madrillet BP 12  
76801 Saint-Etienne du Rouvray Cedex France

Tel: +33 2 32 95 97 84

Email: frederic.grisch@coria.fr

## 1. Introduction

The strategic challenges of the air transport market are very important. With the economic development of many emerging countries and the overall rise in living standards, an expected growth of 100 % in air traffic is expected by 2050. This forecast being more or less formal represents a real unprecedented economic opportunity for aeronautical motorists but also brings many challenges.

To date, the combustion of petroleum, and specifically kerosene (Jet A1), represents the medium-term source of energy to meet a significant growth in air transport. However, a massive use of hydrocarbons in this sector is not without consequences. Indeed, air transport has long been exempted from drastic environmental standards because it was considered negligible compared to road and maritime transports. Today and in the future, the share of responsibility of the air transport sector in global warming will increase significantly and new regulations, increasingly restrictive, were promulgated by the regulatory legislators in this sector. For instance, the Advisory Council for Aeronautical Research in Europe (ACARE) identified new gradual regulations required for the aeronautics industry for 2050 to reduce by 75 % the CO<sub>2</sub> emission per passenger kilometre and NO<sub>x</sub> by 90 %, relatively to the emissions of aircraft produced in 2000 [1].

Reaching the ACARE goals will only be possible by developing novel combustion technologies and by pushing them towards their limitations in regard to the reduction of pollutant emissions and the preservation of the engine operability. Among these technologies are the DAC (dual annular combustor), RQL (Rich burn, Quick-mix, Lean burn), LPP (Lean Premixed Prevaporized), LP (Lean Premixed) and more recently, the multi-point injection or LDI (Lean Direct Injection) architectures [2, 3]. All these technologies are based on staged lean combustion concepts that are intended to reduce the flame temperature and to improve the fuel-air mixing, that limits the production of NO<sub>x</sub> [4]. However, an operation in a lean burn regime can raise problems in terms of flame extinction limit, altitude relight, thermo-acoustic stability and pollutant emissions.

As a consequence, it is mandatory to investigate in the smallest details most of the various physical and chemical mechanisms that govern turbulent spray combustion in relation with the architecture of the injection device installed inside the combustion chamber. To better

1 understand the interplay of physical mixing and chemical kinetic processes ~~able of making~~  
2 ~~mutually~~ an overall lean, low-NO<sub>x</sub> operation and a flame stability, high-fidelity device-scale  
3 modelling capabilities such as numerical Large-Eddy simulation (LES) have been developed,  
4 ~~these ones being~~ currently mature to perform a pre-sizing of the architecture of combustion  
5 chambers. However, even if large-scale simulations predict the spatial and temporal dynamics  
6 of the turbulent flows as well as their reactive structures, significant deficiencies in predictive  
7 capabilities of existing pollutant formation models for high-pressure kerosene combustion are  
8 still noted because of the limited understanding of these processes [5]. To overcome this  
9 limitation, optical measurement diagnostics suited for engine-relevant conditions need to be  
10 developed and implemented in multi-phase flows to provide detailed information on many  
11 scalar parameters and if possible quantitatively. Furthermore, efforts on the combination of  
12 these diagnostics must also be privileged to correlate the scalar quantities measured  
13 simultaneously. Within a close collaboration between the French CORIA laboratory and the  
14 French ~~motorist~~ Safran, an industrial chair called PERCEVAL (*Powering the Future for Clean*  
15 *and efficient aero-engines*) was created and launched to perform experimental, numerical and  
16 technological studies of high-pressure swirl lean premixed kerosene/air combustion issued  
17 from novel industrial Low-NO<sub>x</sub> injection systems [6].

18 To illustrate the capabilities of such studies, the current paper provides a comparison between  
19 experimental and numerical results for a full sized advanced lean premixed injection system  
20 (LP) fed with liquid kerosene (Jet A1). Experiments were performed in the HERON (*High*  
21 *pressure facility for aero-engines combustion*) test facility in the 0.4 – 1.8 MPa pressure range  
22 [7, 8]. Various laser diagnostics such as PIV, OH-PLIF and kerosene-PLIF were used to provide  
23 useful data to study the interplay between the aerodynamics and the flame structure and fuel  
24 distribution. PDA measurements in reactive conditions were also performed to measure the  
25 distribution of the fuel droplet size at the exit of the injection system, parameters which are  
26 key points to define the inlet conditions for the liquid fuel in the numerical predictions. To  
27 enhance our understanding on the mechanisms occurring in the NO<sub>x</sub> formation,  
28 measurements of the distributions of nitric oxide (NO) by Planar Laser-induced Fluorescence  
29 (PLIF) were also performed and correlated to the other scalar parameters measured  
30 previously. Finally, a demonstration of temperature measurements with the novel CPP fs-

1 CARS diagnostic operating in the femtosecond regime in high-pressure conditions will be  
2 presented and discussed.

3  
4 In connection with experiments, a second phase of the research work has been to set up,  
5 perform and post-process simulations of the same test conditions than studied  
6 experimentally. To this end, the YALES2 numerical solver was used. This one is dedicated to  
7 the LES of turbulent reactive flows on unstructured grids at low-Mach number [9, 10]. YALES2  
8 has been specifically tailored for exploiting massively parallel computers and the handling of  
9 meshes with billions of cells [37]. One specific interest of this study has been to find the  
10 relationship between the atomization process, the evaporation of the fuel droplets and the  
11 flame topology. A numerical parametric study on the inlet fuel droplet distributions injected  
12 at the exit of the injector was therefore performed to evaluate their effects on the flame  
13 properties. Results of this parametric study performed with four distinct inlet fuel droplet size  
14 distributions were then compared with the experimental data to increase our understanding  
15 on the validity of the LES combustion solvers that will be used in the future to develop and  
16 validate the predictive capability of novel airbreathing combustors.  
17  
18  
19  
20  
21  
22  
23  
24  
25  
26  
27  
28  
29

## 30 **2. High-pressure combustion facility**

31 Experiments were conducted on the HERON combustion facility that was designed to  
32 investigate novel low-NO<sub>x</sub> full-scale injection systems for helicopter combustors up to their  
33 full operating ranges and airplanes combustors up to 2/3 of their nominal ranges. A detailed  
34 description of the design including the peripheral equipment, and the specifications of the  
35 test facility and its supply and operation environment can be found in [7, 8]. Here, only the  
36 salient features of the combustion test facility are given. A schematic of the test facility can  
37 be found in Fig. 1.  
38  
39  
40  
41  
42  
43  
44  
45

46 The water-cooled optical segment is a square duct of 100 mm inner dimension, made of  
47 stainless steel and fitted with four fused silica windows for optical access. Both lateral optical  
48 windows are 80 mm long and 100 mm high so that the entire region of the flame can be  
49 observed in the test chamber. Two complementary upper and lower optical windows of 80  
50 mm long and 30 mm wide complete the optical access. The inner surface of the windows is  
51 protected by preheated air films injected by thin slots arranged around the burner faceplate  
52 in which the injection system is fixed. Further downstream, the visualization segment, a sensor  
53  
54  
55  
56  
57  
58  
59  
60  
61  
62  
63  
64  
65

1 module equipped with various measurement transducers is placed. A pressure transducer  
 2 ensures the record of dynamic pressure fluctuations into the combustion chamber while  
 3 several thermocouples of type K are used to control the temperature of the reactive flow and  
 4 the walls of the combustion chamber. Then a dilution segment designed to convert the square  
 5 section of the combustion chamber toward a circular section, takes place. Additional dilution  
 6 air at room temperature is injected through eight radial pipes positioned on the dilution  
 7 segment for cooling the hot gases by mixing. Finally, the outlet of the combustor is equipped  
 8 with an adaptive sonic throttle which can be gradually obstructed by a water-cooled needle  
 9 in order to precisely monitor the pressure inside the combustor. Exhaust gases are then  
 10 collected by a fan to be extracted outside the building. The combustion chamber is supplied  
 11 with compressed air preheated electrically. The combustion facility is designed for operation  
 12 of fuel injectors at up to 2.0 MPa and 900 K, with a maximal air flow rate of 300 g/s.  
 13  
 14  
 15  
 16  
 17  
 18  
 19  
 20  
 21  
 22  
 23

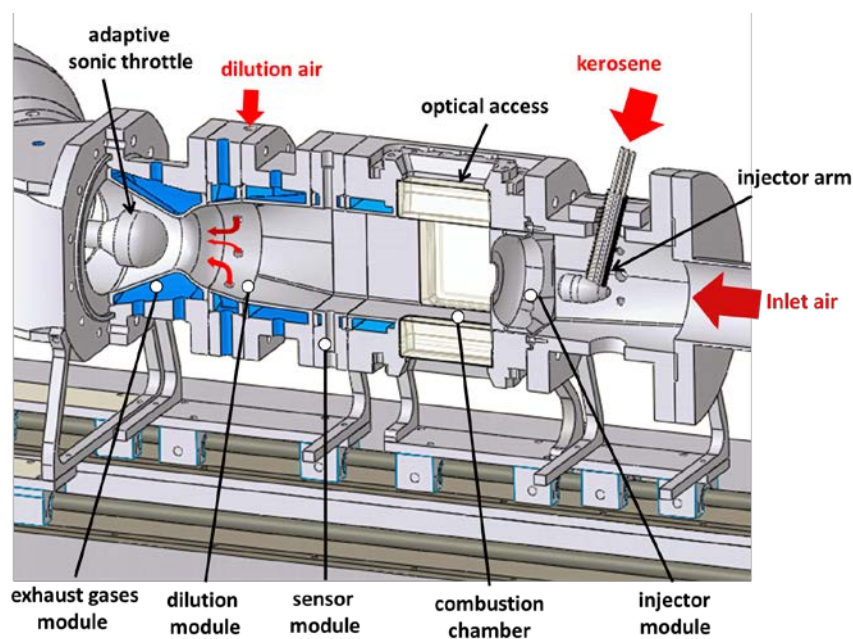


Fig. 1: Schematic of the HERON test facility

The lean premixed fuel injection system combines swirl spray and multi-hole injection functions. It was expected that those two functions would provide beneficial effects to the fuel injector for improving the fuel/air mixture. This effect considerably reduces the length of the flame and improves the flame stability. The fuel injection consists of a central nozzle pierced with height holes on the side wall, identical in diameter to the central orifice. Part of the fuel is injected through the central hole and atomized by the central swirling airflow via



1 an airblast atomization concept. This atomization creates a rich zone of liquid droplets that  
2 helps to the stabilization of the flame. The second part of the fuel flow is injected through the  
3 side ports. The resultant droplets produced via a liquid jet in crossflow process can either  
4 impact the internal wall or be carried away by the internal swirling air flow. Note that a special  
5 feature of this multipoint injector is that the lateral/central fuel injection ratio is not  
6 controlled, but this one is kept constant in relation with the geometry of the injector. In the  
7 event that part of the kerosene droplets impacts the wall facing the lateral holes, a liquid film  
8 can be created and carried away by the air stream. The liquid film is then torn off and finely  
9 atomized, creating an external conical zone, where air and partially evaporated fuel mix  
10 together. The air/fuel mixing is finally sheared between two swirled air flows to be  
11 homogenised prior to be ejected into the combustion chamber.  
12  
13  
14  
15  
16  
17  
18  
19  
20  
21

### 22 **3. Experimental methods**

#### 23 ***3.1 Phase Doppler Anemometry***

24 The two-phase flow structure and particle dispersion at the exit of the injection system were  
25 experimentally investigated by means of the Phase Doppler Anemometry (PDA) optical  
26 technique [11, 12]. To this end, a Dantec Dynamics dualPDA system was used to measure the  
27 spatio-temporal droplet size-velocity profiles in the flame. It consists of an emitting part, a  
28 receiving part, and a signal processor. The emitting system includes two 1W diode lasers,  
29 model Genesis MX 488-1000 SLM and Genesis MX 514-1000 SLM. After that the diameters of  
30 the laser beams at 488 and 514 nm were set to 2.2 mm with an expander ratio of 1.98, a shift  
31 frequency of 40 MHz was generated by passing one of the laser beams through a Bragg cell.  
32 Both laser beams are then conducted through fibre optics and transmitted towards the probe  
33 volume via a Dantec FiberFlow optical system. Adopting an emitting focal length of 350 mm  
34 and a beam spacing of 40 mm, the probe volume with a length of 350  $\mu\text{m}$  and a diameter of  
35 50  $\mu\text{m}$  is generated. The noise and reflected light contributions able to disturb the detection  
36 of the burst signal were minimized by fixing the receiving optical system at 30° to the forward  
37 scattered direction. The detection system consists of a 112 mm diameter DualPDA receiving  
38 probe in which the focal length of the receiver is 310 mm. Within its specifications, this setup  
39 was optimized to measure droplets within the range of diameters of 1 – 60  $\mu\text{m}$ . The  
40 measurement signal is transmitted by optical fibres to the detector unit. The transmitting and  
41 receiving optics were mounted on a computer-controlled 3D traversing system and the  
42  
43  
44  
45  
46  
47  
48  
49  
50  
51  
52  
53  
54  
55  
56  
57  
58  
59  
60  
61  
62  
63  
64  
65

1 measurements were performed at various positions along the axial and radial directions  
2 downstream from the nozzle exit.  
3

4 The location of the measurement planes in the spray were defined by the axial distance from  
5 the injector (Z) and the radius (Y), with an origin defined as the nozzle exit. For the current  
6 study, PDA measurements were performed on X-Y planes at  $Z/D = 0.04$  and  $0.64$  from the  
7 injector. At  $Z/D=0.04$ , a quarter of the flow exit cross-section was probed adopting a cartesian  
8 grid with  $\Delta X=0.25$  mm and  $\Delta Y=1$  mm while at  $Z/D=0.64$ , polar coordinates with  $\Delta\theta=10^\circ$  and  
9  $\Delta Y=1$  mm were selected to mesh the grid. For each measurement location, the PDA signals  
10 were processed with a Burst Spectrum Analyzer (BSA) P80 processor. The acquisition time for  
11 each measurement was set to 30 seconds or by fixing a maximal data sampling of 10000  
12 droplets. These settings helped an estimation of the accurate droplet size and velocity  
13 statistics. In the current study, the PDA validation rate is  $\sim 90\%$ . The measurement accuracy  
14 of the velocity is about  $5\%$  and of the size about  $10\%$  of the measured value.  
15  
16  
17  
18  
19  
20  
21  
22  
23  
24  
25

### 26 **3.2 High-speed Particle Image Velocimetry**

27 Velocity measurements in reacting flows were performed using high-speed PIV for  
28 investigating the effect of pressure on the aerodynamics [13]. The PIV measurements were  
29 performed using a dual-cavity high-speed Nd:YLF laser (Quantronix Darwin Dual 80) operating  
30 at a repetition rate of 10 kHz with a pulse energy of 2.4 mJ. The temporal separation between  
31 the independent pulses was fixed to  $5\ \mu\text{s}$ . This value was optimized in order to simultaneously  
32 capture high velocity vectors in the jet zones and low velocity vectors into the internal  
33 recirculation zone. The emitted laser beam then passes through the sheet forming optics (one  
34 spherical and two cylindrical lenses) to expand it into a parallel sheet and align it along the  
35 flow axis of the reactive flow. The dimensions of the laser sheet formed a 50 mm (tall) x 0.5  
36 mm (thick). The reactive flow was seeded with  $\text{ZrO}_2$  particles  $5\ \mu\text{m}$  in diameter by means of a  
37 cyclone seeding device specially designed to operate in high-pressure conditions. For practical  
38 reasons,  $\text{ZrO}_2$  particles were mixed with  $1\%$  wt of submicrometric  $\text{SiO}_2$  particles ( $0.2\ \mu\text{m}$  in  
39 diameter). This procedure was used to improve the homogeneity of the seeding inside the  
40 combustor by preventing any formation of agglomerates under the action of humidity.  
41  
42  
43  
44  
45  
46  
47  
48  
49  
50  
51  
52  
53  
54  
55

56 The Mie scattering signals generated by particles were collected and detected using a CMOS  
57 high-speed camera (Phantom V2512) equipped with a Zeiss Milvus 2/100M 100 mm lens  
58  
59  
60  
61  
62  
63  
64  
65

1 (f/2.8) and a narrow bandpass filter centred at 527 nm. The camera operated in the exposure  
2 PIV mode function at 20 kHz, with a camera resolution of 1600 x 1200 pixels. A final field of  
3 view of 50 x 50 mm<sup>2</sup> was recorded and data processed using the Dynamics Studio software. A  
4 multi-pass adaptive cross-correlation with an interrogation window size decreasing from 64 x  
5 64 to 16 x 16 pixels with a 50% overlap was used to measure the displacement of particles.  
6 This results in the determination of 80 x 50 velocity vectors spaced of 1.14 mm.  
7  
8  
9  
10

### 11 **3.3 Low-speed OH-PLIF and Kerosene-PLIF**

12 The measurement strategy used to detect simultaneously OH and kerosene vapor  
13 fluorescence inside the high-pressure flame, describing the experimental setup and the  
14 specifications of the data processing of measurements to measure the quantitative molar  
15 fraction and temperature of kerosene vapor can be found in [14]. Here, only the salient  
16 features of the experimental setup are given.  
17  
18  
19  
20  
21  
22  
23  
24

25 The methodology used to perform kerosene vapor measurements in high-pressure conditions  
26 ~~was relying on~~ that the kerosene vapor fluorescence signal via a single-photon excitation at  
27 266 nm shows two distinct spectrally broadband fluorescence signals in the spectral ranges  
28 270-310 nm and 310-410 nm. These spectral domains are associated to the fluorescence of  
29 mono-aromatics and di-aromatics compounds respectively. It ~~was~~ also well known that the  
30 intensity of the kerosene fluorescence decreases faster with the increase of temperature for  
31 the high-frequency ~~band~~ than for the low-frequency ~~and~~ and this difference ~~will be~~ used as the  
32 principle to process both fluorescence signals in terms of kerosene mole fraction and  
33 temperature. Experimentally, the measurement strategy consisted to excite aromatics  
34 included in the species composition of kerosene by a conventional one-photon excitation and  
35 the photon was generated by a frequency-quadrupled Nd:YAG laser. The collection of both  
36 fluorescence signals was performed via a dual-wavelength detection strategy. The resultant  
37 output pulse energy at 266 nm was 60 mJ per pulse at the exit of the laser source. The  
38 kerosene-PLIF and OH-PLIF diagnostics were then coupled to get simultaneous detailed  
39 correlation on the flame structure and fuel vapor distribution at the exit of the injection  
40 system, that was fruitful to study the correlation between the consumption of kerosene vapor  
41 and the production of OH radicals. To this end, a Nd-YAG-laser operating at 532 nm was used  
42 to pump a tuneable dye laser (SIRAH Precision Scan) supplied with Rhodamine 590 dye at a  
43 repetition rate of 10 Hz for detecting OH radicals. The resultant output pulse energy was 25  
44  
45  
46  
47  
48  
49  
50  
51  
52  
53  
54  
55  
56  
57  
58  
59  
60  
61  
62  
63  
64  
65

1 mJ per pulse at the exit of the laser source. The excitation wavelength was tuned to the  $Q_1(5)$   
2 transition line of the  $A^2\Sigma^+(v' = 1) \leftarrow X^2\Pi(v'' = 0)$  band of OH at  $\lambda = 282.75$  nm. Time delay between  
3 both laser beams was then fixed to 60 ns in order to avoid cross-talks between the  
4 fluorescence signals of OH and kerosene. Both laser beams were superimposed with a prism  
5 and they were transformed into two superimposed collimated sheets using a set of cylindrical  
6 and spherical lenses. The collection system for OH measurements consisted of an emICCD  
7 camera (PIMAX 4, Roper Scientific) with two coloured glass filters (WG295 and UG5) and an  
8 interferential filter centred at 310 nm (FWHM = 5.6 nm). The camera was slightly tilted from  
9 the perpendicular axis and equipped with a Sheimpflug mount in order to put in place the two  
10 16-bit emICCD cameras equipped with a 100 mm, f/2.8 UV-CERCO lens for the detection of  
11 kerosene signals. The first camera was equipped with a combination of coloured glass filters  
12 to collect the whole fluorescence of kerosene, whereas the second camera used a combination  
13 of optical filters to collect fluorescence from di-aromatics only. For kerosene/di-aromatics  
14 images, the signal emitted from the kerosene droplets was suppressed and replaced by the  
15 fluorescence signal of the vapor around them. PLIF images were corrected by noise, laser  
16 sheet energy inhomogeneity, and distortion using the DaVis 8.1 commercial software.

### 31 **3.4 Low-speed NO-PLIF and OH-PLIF**

32 A coupling of OH-PLIF and NO-PLIF systems was developed to simultaneously image the NO  
33 and OH distributions inside the high-pressure combustor [15]. This experimental setup  
34 consists of the combination of two PLIF systems located in a room close to the test bench. The  
35 OH-PLIF system consisted of a frequency-doubled dye laser pumped by a Q-switched Nd:YAG  
36 laser. The laser was tuned to the  $Q_1(5)$  rotational transition of the  $A^2\Sigma^+ \leftarrow X^2\Pi(1,0)$  band of OH  
37 at 282.75 nm, with a pulse energy of 16 mJ. The laser linewidth was measured to be  
38 approximately 0.06 cm<sup>-1</sup> by recording the fluorescence spectral profile of the OH transitions  
39 in a premixed CH<sub>4</sub>-air reference flame stabilized over a porous burner (Mac-Kenna). This  
40 rotational line was selected because of its propensity to deliver a fluorescence signal  
41 presenting a weak temperature sensitivity.

42 For NO-PLIF, the 532 nm laser beam generated from an injection seeded frequency-doubled  
43 Nd:YAG laser was used to pump a Sirah Precision scan LG-2400 dye laser operating with a  
44 mixture of Rhodamine B and Rhodamine 590 dyes. The 615 nm output of the dye laser was  
45 sum-frequency-mixed with the third-harmonic beam of the Nd:YAG laser to produce the  
46  
47  
48  
49  
50  
51  
52

1 225.12 nm radiation required to probe NO via a one-photon excitation process. Generation of  
2 wavelengths around 226 nm by the mixing process was favoured to the “conventional”  
3 frequency doubled blue dyes pumped by the third-harmonic beam of the Nd:YAG laser  
4 because of its predisposition to deliver longer lifetime for the dyes, a smaller spectral  
5 bandwidth for the UV radiation and a generation of high energy/pulse (up to 30 mJ). As for  
6 OH-PLIF measurements, the laser beam wavelength was tuned to the  $Q_1(29.5)$  rotational  
7 transition. The linewidth was then estimated to be  $\sim 0.07 \text{ cm}^{-1}$ . This rotational line was  
8 selected as a convenient way to produce strong fluorescence signal and to be relatively  
9 insensitive to variations in temperature. Both laser beams were transported and  
10 superimposed via optical mirrors around the combustion chamber and superimposed with  
11 dichroic mirrors. They were then transformed into two collimated laser sheets using a set of  
12 two cylindrical and one spherical lens. The first two lenses (-20 mm and 300 mm focal lens)  
13 formed a cylindrical telescope which spread the beams into two collimated 5 cm tall planar  
14 laser sheets. The spherical lens with 1 m focal length focused the laser sheets into a  $\sim 130 \mu\text{m}$   
15 waist located in the centre of the combustor. Energy in the laser sheets were maintained to 4  
16 mJ for OH and 6 mJ for NO experiments, respectively in order to stay in the linear regime.  
17 Fluorescence from OH and NO were recorded on two 16-bit em-ICCD cameras (PIMAX4)  
18 equipped with CCD chip offering a maximum resolution of  $1024 \times 1024$  pixels. An exposure  
19 time of 70 ns was chosen for all the LIF recordings presented in this work and the framing rate  
20 of each laser PLIF setup was fixed to 10 Hz. For OH measurements, the camera was equipped  
21 with a WG 295 filter associated with an interferential filter centred at 315 nm (FWHM = 15  
22 nm). The NO LIF signals were filtered using a series of filters allowing the detection of signals  
23 in the 225 – 300 nm spectral domain while rejecting the laser scattering and kerosene  
24 fluorescence signals that would otherwise appear in the LIF recordings. As kerosene has a  
25 continuous absorption spectrum in the spectral domain in which NO is excited, there is a  
26 possibility for which NO and kerosene LIF can be excited together with the 226 nm pulse beam.  
27 To discriminate NO and kerosene fluorescence during the post-processing of the  
28 measurements, kerosene-LIF signals were also collected on a third em-ICCD camera mounted  
29 with a 100 mm, f/2.8 UV-objective (Cerco). A stack of two WG305 filters combined with a  
30 custom-made bandpass filter collected the kerosene fluorescence in the 300 - 400 nm spectral  
31 range. Each camera was interfaced to a PC computer used to control the cameras and acquire  
32 the PLIF images. The gain of each em-ICCD camera was adjusted to prevent local saturation  
33  
34  
35  
36  
37  
38  
39  
40  
41  
42  
43  
44  
45  
46  
47  
48  
49  
50  
51  
52  
53  
54  
55  
56  
57  
58  
59  
60  
61  
62  
63  
64  
65

1 while maximizing the fluorescence signals. Shot-to-shot laser energy variations were  
2 accounted for during the measurements by two photodiodes recording the fluctuations of the  
3 energy of both pulse lasers during the experiments. Raw fluorescence images were corrected  
4 for background luminosity, non-uniformities in the collection optics and inhomogeneity in the  
5 laser sheet profile. An average background image was acquired in air flow with laser on.  
6 Subtraction of this image from the fluorescence image accounts for laser scattering and other  
7 background luminosity. 500 instantaneous PLIF images for each species were recorded at a  
8 sampling rate of 3.33 Hz.  
9

### 10 **3.5 CPP fs-CARS**

11 The CARS laser diagnostic is a third-order nonlinear optical process widely used to obtain gas-  
12 phase temperature measurements. CARS experiments and theory can be found in the  
13 literature reviews and textbooks [16-18]. Recognized as an unavoidable diagnostic with  
14 nanosecond laser arrangements, a new interest for CARS has recently arisen with the  
15 availability of femtosecond laser sources [19, 20]. A new interaction regime due to ~100 fs  
16 excitation laser pulses reduces non-resonant signal interferences with the resonant CARS  
17 signal. Moreover, the high laser energy delivered by the femtosecond laser makes single-shot  
18 temperature measurements accessible and taking interest of a repetition rate up to 10 kHz,  
19 thousand times larger than in the nanosecond regime offering then the study of dynamic  
20 processes. In the current study, single-shot N<sub>2</sub> CPP fs-CARS spectra were recorded in the high-  
21 pressure test facility to demonstrate the potential to perform high-speed single-shot  
22 temperature measurements in high-pressure reacting conditions. The CPP fs-CARS  
23 experiments were conducted with a Ti:Sapphire femtosecond laser system consisting of an  
24 oscillator (Coherent Vitesse) combined to an amplifier (Coherent Legend Elite Duo HE + III)  
25 which delivered pulses of ~95 fs (FWHM) duration at 800 nm at a repetition rate of 1 kHz. The  
26 oscillator source provided short pulses of few nJ at a frequency rate of 80 MHz. Amplification  
27 was performed by a CPA (Chirped Pulse Amplification) system consisted of a stretcher which  
28 temporally expands the pulse and reduce its peak power, followed by two amplification  
29 stages. The first amplification stage consisted of a multi-passage cavity optically pumped by a  
30 23 W laser source (Coherent Evo 45) to deliver an energy of ~7.5mJ. The second stage was  
31 optically pumped with a counter-propagative process by a second 45 W laser source (Coherent  
32  
33  
34  
35  
36  
37  
38  
39  
40  
41  
42  
43  
44  
45  
46  
47  
48  
49  
50  
51  
52  
53  
54  
55  
56  
57  
58  
59  
60  
61  
62  
63  
64  
65

1  
2  
3  
4  
5  
6  
7  
8  
9  
10  
11  
12  
13  
14  
15  
16  
17  
18  
19  
20  
21  
22  
23  
Evo HE) to reach in a single pass pulse energy of  $\sim 15.8$  mJ. After a temporal recompression, the resulting energy of the laser pulse was  $\sim 12$  mJ. The output laser beam was then split so that half of the energy of the 800 nm laser beam pumped an Optical Parametric Amplifier (OPA, TOPAS Prime Plus) while the second part was used as the Stokes beam. The output beam from the OPA was at 675 nm and the energy was set to 520  $\mu$ J. The resulting OPA beam was subsequently divided into two parts for producing the pump and the probe beams. The probe beam was chirped by inserting a 30 cm long SF11 glass rod into the beam path for stretching the temporal width of the pulse from 95 fs to 2.5 ps. The temporal coincidence of the pulses at the probe volume was controlled with two motorized linear translation stages installed along the beam path of the pump and the probe beam. Control of energies of the laser pulses at the exit of the CARS setup was adjusted by using neutral density filters and thin-film polarizer and half-wave plates.

24  
25  
26  
27  
28  
29  
30  
31  
32  
33  
34  
35  
36  
37  
38  
39  
40  
41  
The beams were then arranged in a folded BOXCARS configuration and focused into the measurement probe of 1.2 long and 50  $\mu$ m in diameter using a 250 mm focal length lens. The energies deposited into the probe volume for the pump, Stokes and probe pulses were 35  $\mu$ J, 35  $\mu$ J and 210  $\mu$ J respectively. After collimating the CARS signal with a 250 mm focal length lens, this one was spatially and spectrally filtered from the incident laser beams and then transported by mirrors to be focused to the entrance slit of a 0.32 m spectrograph (Princeton Isoplan 320) equipped with a 1200 lines/mm grating. A emCCD camera (ProEM-HS 512x512) which was triggered by the fs-laser time circuit, completed the detection system by imaging the CARS spectra at a repetition rate of 1 kHz.

### 42 **3.6 LES Numerical solver**

43  
44  
45  
46  
47  
48  
49  
50  
51  
52  
53  
54  
55  
56  
57  
58  
59  
60  
61  
62  
63  
64  
65  
Large Eddy simulations (LES) were performed using the flow solver YALES2. The code is an unstructured, multi-physics solver for a wide range of flow problems capable of handling massive hybrid meshes [9, 21]. For the current study, the time integration relied on a low-Mach number projection method for variable density flows. The temporal integration and spatial discretization are of fourth-order. The sub-grid scale Reynolds stresses are closed with the localized dynamic Smagorinsky model proposed by Germano [22]. The tabulated chemistry method retained in the current work is the PCM-FPI method [23], in which the chemical subspaces were modelled by a family of 1-D gaseous laminar premixed flames computed using detailed chemistry for various equivalence ratio within the flammability

limits. PCM-FPI tables were generated using the CANTERA solver associated with the skeletal LUCHE mechanism including 92 species and 694 reactions [24]. Reactions and species concentration were then tabulated as a function of the progress variable ( $Y_{\text{CO}}$  built from a linear combination of the  $Y_{\text{CO}}$ ,  $Y_{\text{CO}_2}$  and  $Y_{\text{H}_2\text{O}}$  species mass fractions and the mixture fraction ( $Z$ ). PCM-FPI tables were finally convoluted with  $\beta$ -PDF functions for considering the sub-grid fluctuations. Considering the two-phase modelling, the Euler/Lagrange approach was selected. The gas phase was represented using the Euler description while the spray phase was defined in a Lagrangian framework. The droplets were assumed to be spherical and the evaporation of droplets was modelled using the Abramzon & Sirignano approach [25]. The droplet distribution injected via the injection system was assumed to be polydispersed in size, following four possible two-parameter Rosin–Rammler particle number distributions [26] defined as:

$$f(D) = \frac{qD^{q-1}}{X^q} \exp\left[-\left(\frac{D}{X}\right)^q\right]$$

$q$  is the spread parameter giving the distribution width,  $D$  is the diameter of the droplets and  $X$  is a characteristic parameter.  $X$  and  $q$  are related by the Sauter mean diameter (SMD or  $D_{32}$ ) equation in which  $\Gamma$  is the incomplete gamma function:

$$D_{32} = \frac{X^3 \Gamma\left(\frac{3}{q} + 1\right)}{X^2 \Gamma\left(\frac{2}{q} + 1\right)}$$

Thus, the input parameters, representing key parameters for the close characterization of the real atomization process are  $D_{32}$  and  $q$ . Four droplets size distributions depicted in Fig. 2 were thus tested in the current study for studying the effect of the boundary conditions on the disperse phase modeling and thereby avoiding the need to simulate the primary atomization. Table 1 gives for each inlet droplet size distribution the Sauter Mean Diameter (SMD) and the spread parameter  $q$  [27].

	<b>D1</b>	<b>D2</b>	<b>D3</b>	<b>D4</b>
<b>D<sub>32</sub> (μm)</b>	32.5	16	12	9
<b>q</b>	3.1	3.1	3.0	3.0

*Table 1: Input parameters for the four droplet size distributions*



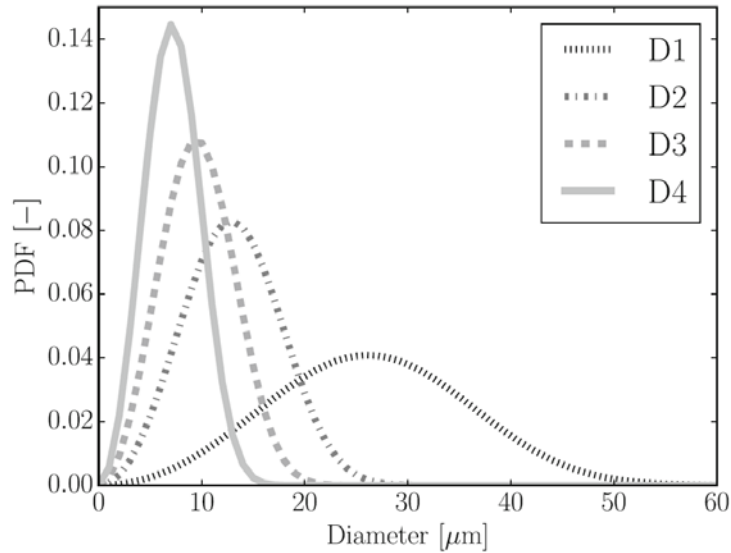


Fig. 2: Rosin-Rammler PDF's distributions

The numerical domain for the simulation of the high-pressure kerosene/air flames covered the full test facility, from the plenum to the exit of the combustion chamber. The mesh was composed of 237 million tetrahedral cells, with a refinement close to the injection channels and reacting zone in which the largest cells were fixed to 250 μm. Note that the prediction of emissions, e.g. NO<sub>x</sub>, were not achieved in the current study as this pollutant cannot be described with the PCM-FPI model without additional models.

## 4. Results

### 4.1 Velocity field in reactive conditions

Flow velocity data using PIV measurements were obtained for pressures ranging from 0.4 to 1.8 MPa for qualitative understanding of the flow structure and the extent of the recirculation zone on the development of the flame structure. The case of the 0.4 MPa pressure condition is characteristic of an idle condition when the helicopter is staying on the runway while the other ones simulate various level of power energy produced by the combustor during the different phases of the flight.

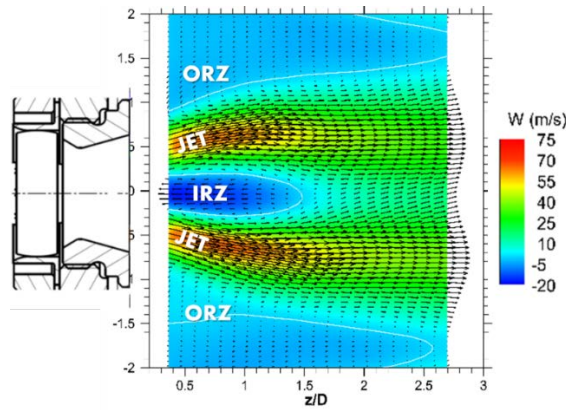


Fig. 3: Experimental velocity distributions in reactive conditions for a pressure of 0.8 MPa

For a pressure of 0.8 MPa, the averaged velocity field is representative of enclosed swirled flames presenting high swirl number (Fig. 3). As expected from a turbulent swirling flow in sudden expansion burner, two distinct regions are discernible [28, 29]. The first, a cone-shaped inner recirculation zone (IRZ) appears as a result of the vortex breakdown. This recirculation region is deeply involved in the flame stabilization process, as it constantly transports hot burnt gases in contact with fresh gases providing permanent ignition. The second, an outer recirculation zone (ORZ) occurs above the shear mixing layer and takes its shape from the neighbouring boundary walls. Between these two zones are located the annular jet flow for which the maximum velocity is up to  $70 \text{ m}\cdot\text{s}^{-1}$  and two annular shear layers denoting as the outlet shear layer (OSL) and the inner shear layer (ISL) that separate the ORZ and the jet inner flow and IRZ and the inner jet flow respectively. We can also observe the presence of negative velocities relatively high ( $\sim -10 \text{ m}\cdot\text{s}^{-1}$ ) in IRZ arising from the efficient transport of burnt gases back towards the injection system by the inner reverse flow. Close to the injector exit plane ( $z/D = 0$ ), velocities are always negative, suggesting that the stagnation point is located inside the injection system bowl.

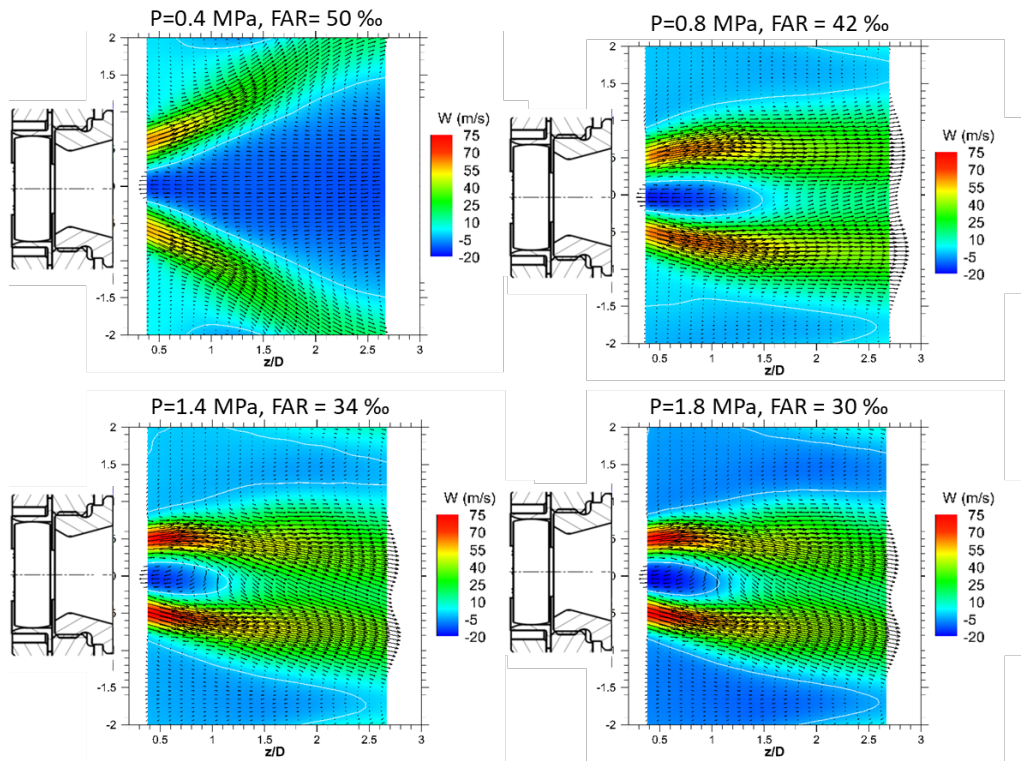
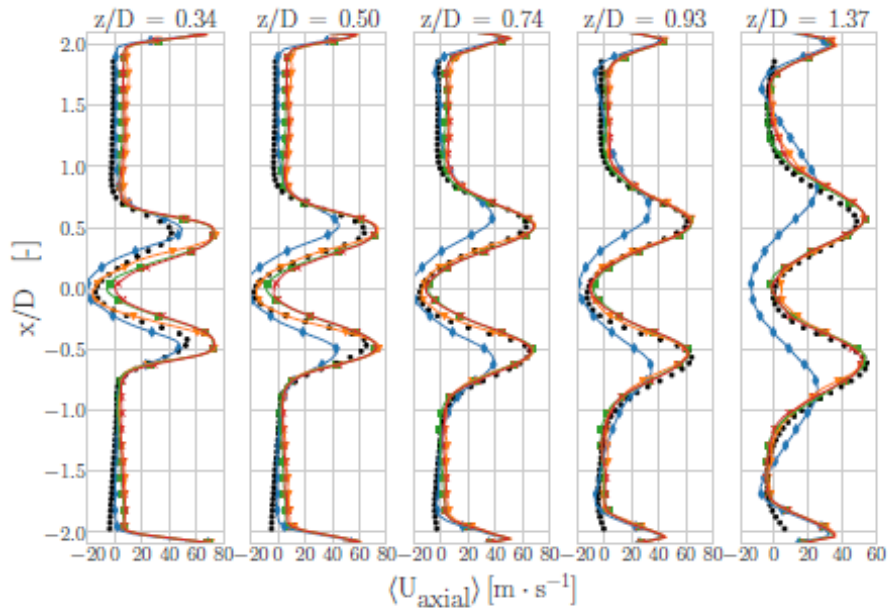


Fig. 4: Experimental velocity distributions for various conditions of pressure and FAR

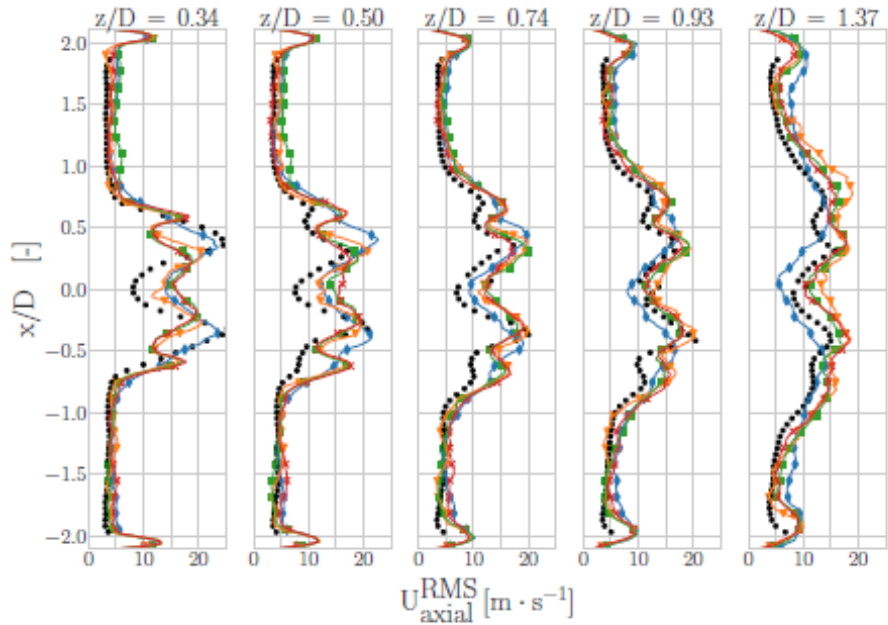
As shown in Fig. 4, the increase of pressure reveals an averaged velocity flow distribution similar to the one observed at 0.8 MPa. The air flow preserves its structure while the gradual increase of the global mass flowrate with pressure generates larger velocities inside the jet zone. A reduction of the length of IRZ with pressure is also observed. This change in flow topology seems the result to a faster evaporation of liquid kerosene with pressure which induces a shifting of IRZ under the action of combustion starting earlier into the bowl. Finally, a slight dissymmetry of the flow is observed on the velocity distributions, this one being probably imputable to the fixing element of the injection system into the plenum which generates a weak distortion of the homogeneity of the boundary conditions of the inlet air/fuel flow before to penetrate inside the combustion chamber. On the other hand, at  $P = 0.4$  MPa, the flow structure is significantly modified. The angle formed by the jet zone opens wide and impacts the walls of the combustion chamber. As a result, the IRZ has a much larger volume and expands sharply along the axial direction of flow.

In Figs. 5 and 6, the numerical mean axial and radial velocity and its rms fluctuations are compared with the experimental velocities for various planes in the axial direction. Whatever the inlet droplet distributions, the numerical predictions globally are in good agreement with

1 the experimental results with the presence of negative velocities along the flow axis denoting  
2 the location of the CRZ and two positive axial velocity peaks characteristics of the penetration  
3 of the jet flow into the combustion chamber. A detailed observation of the numerical results  
4 also displays that the  $D_3$  and  $D_4$  size droplet distributions provide a better agreement between  
5 the experimental and numerical data. The fluctuations of the axial velocity represented in Fig.  
6 5b are correctly captured along the chamber, even if the numerical values are slightly  
7 underestimated for the measurement plane close to the nozzle exit. Finally, the numerical  
8 solver with the different inlet droplet size distributions globally captures the radial velocity  
9 profiles for all the measurements planes, except for the  $D_1$  and  $D_2$  distributions for which  
10 larger gradients of velocity appear in ORZ.  
11  
12  
13  
14  
15  
16  
17  
18  
19  
20  
21  
22  
23  
24  
25  
26  
27  
28  
29  
30  
31  
32  
33  
34  
35  
36  
37  
38  
39  
40  
41  
42  
43  
44  
45  
46  
47  
48  
49  
50  
51  
52  
53  
54  
55  
56  
57  
58  
59  
60  
61  
62  
63  
64  
65

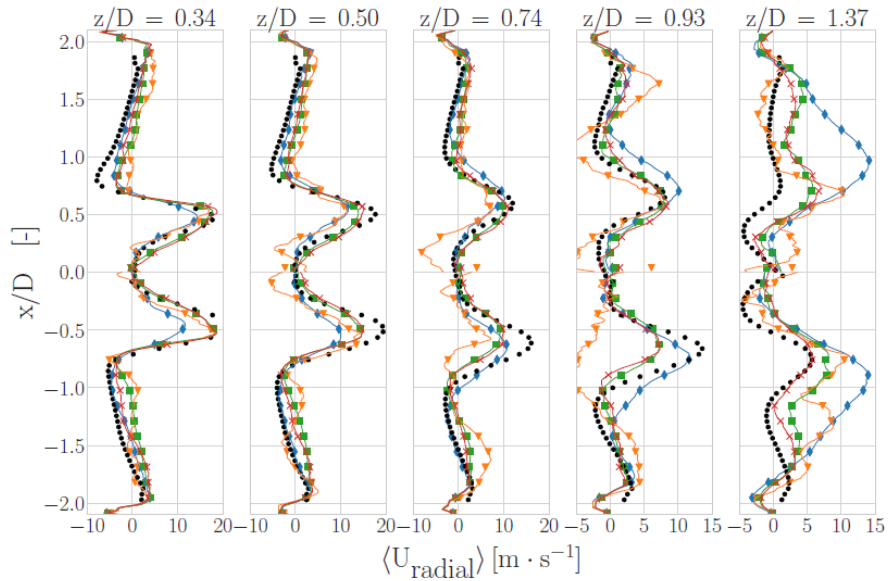


(a)

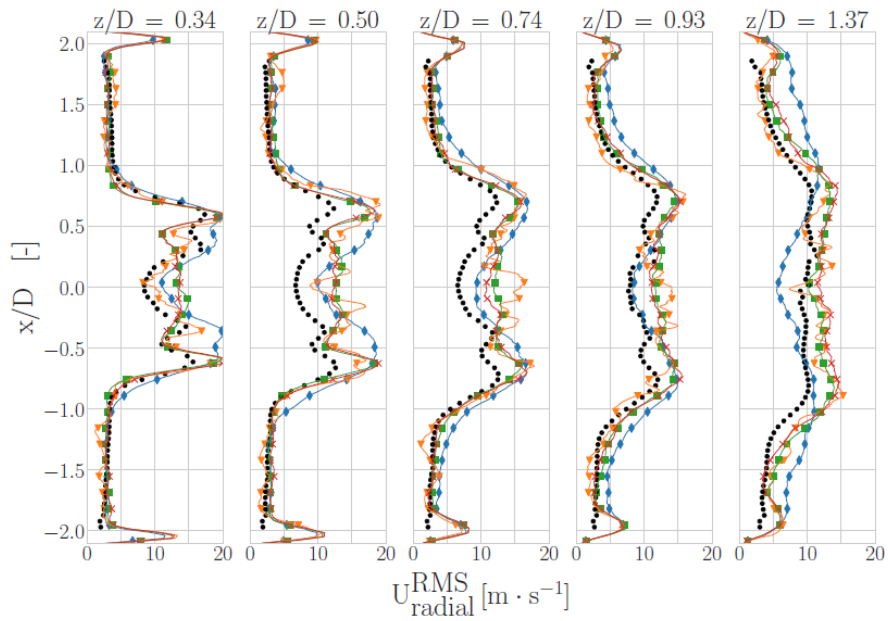


(b)

Fig. 5: Mean (a) and rms (b) of the axial gas velocity as a function of radial position for different distances from the injection system. Experimental data ( $\bullet$ ), numerical predictions for the D1 ( $\blacklozenge$ ), D2 ( $\blacktriangledown$ ), D3 ( $\blacksquare$ ) and D4 ( $\blacktimes$ ) inlet droplets size distributions.



(a)



(b)

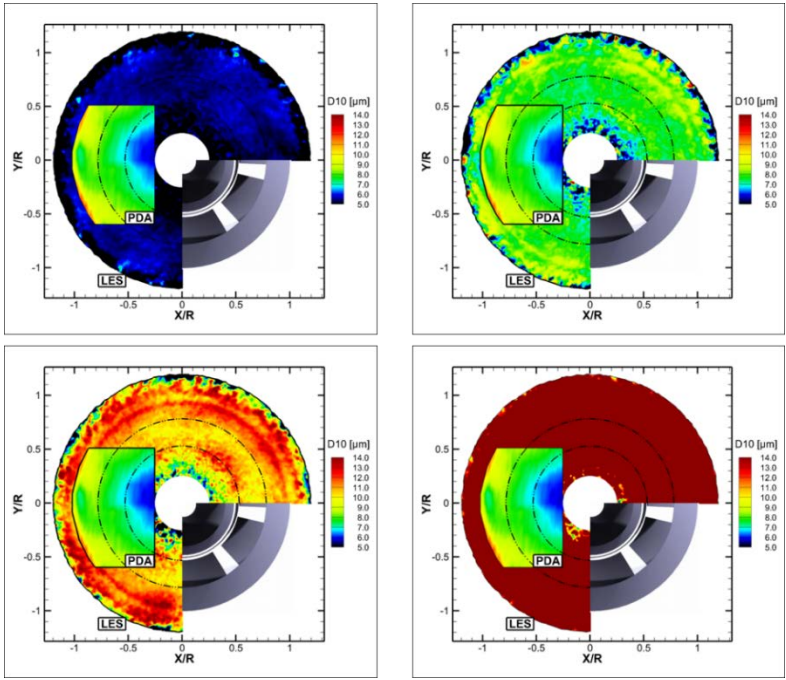
Fig. 6: Mean (a) and rms (b) of the radial gas velocity as a function of radial position for different distances from the injection system. Experimental data ( $\bullet$ ), numerical predictions for the D1 ( $\blacklozenge$ ), D2 ( $\blacktriangledown$ ), D3 ( $\blacksquare$ ) and D4 ( $\blacktimes$ ) inlet droplets size distributions.

## 4.2 Spray topology

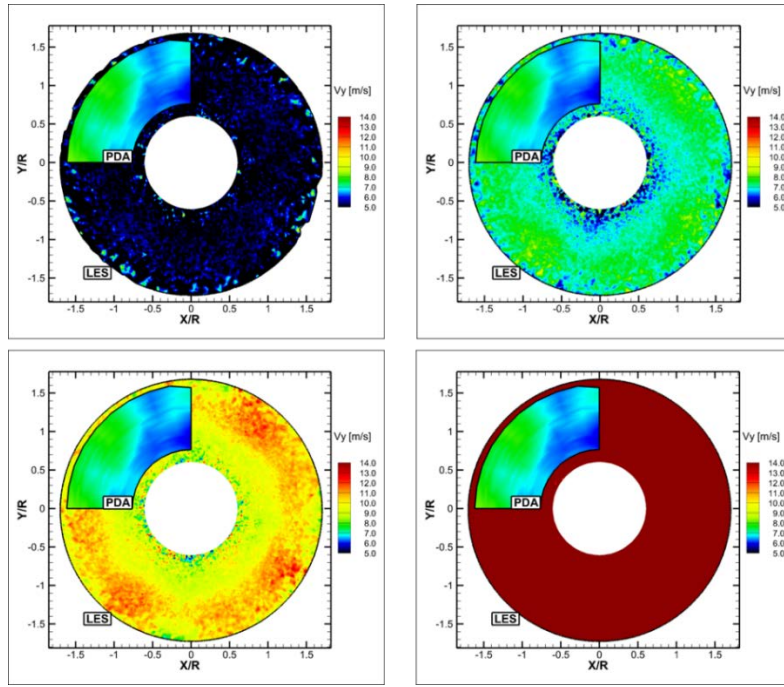
Detailed measurements of the mean diameter  $D_{10}$  of kerosene droplets distributions using PDA were performed in reactive conditions at a pressure of 0.83 MPa and the resultant distributions are displayed in Fig. 7 for two measurements planes downstream from the



injector. These two planes correspond to  $Z/D = 0.04$  and  $Z/D = 0.64$  where the numerical results could be compared to experimental results. Starting with results at  $Z/D = 0.04$ , the numerical simulation with the  $D_1$  droplet distribution produces droplets much larger than those observed in the experiments. The  $D_2$  droplet distribution gives also droplets that are bigger than the ones measured in the real spray again. For the  $D_3$  droplet distribution, a good agreement is obtained between the numerical and the experimental results. In both cases, the smallest droplets are located in the central part of the spray, while the largest droplets are located outside. Finally, the  $D_4$  distribution features much smaller droplets than in the experimental case. Moving at  $Z/D=0.64$ , both  $D_1$  and  $D_2$  distributions exhibit too large diameters. On the contrary, the droplet distribution calculated with the  $D_3$  droplet distribution reproduces the history of the transport and evaporation of the drops in the flow and match well the experimental results, with some clusters of bigger droplets in the outer part of the spray. The only difference between the experimental and numerical results lies into the droplets distributions which are less homogenous numerically. This is only due to the smaller number of droplets that arrive to this plane. A lower number of droplets may be the consequence of the numerical parcel approach used to simulate the properties of the spray. However, this procedure could not be easily evaluated.



(a)



(b)

Fig. 7: Radial distributions of the  $D_{10}$  mean diameter of droplets at  $Z/D = 0.04$  (a) and  $Z/D = 0.64$  (b). Results recorded in reactive conditions are compared to LES simulations with the four inlet droplets size distributions ( $D_1$ ,  $D_2$ ,  $D_3$  and  $D_4$ ).

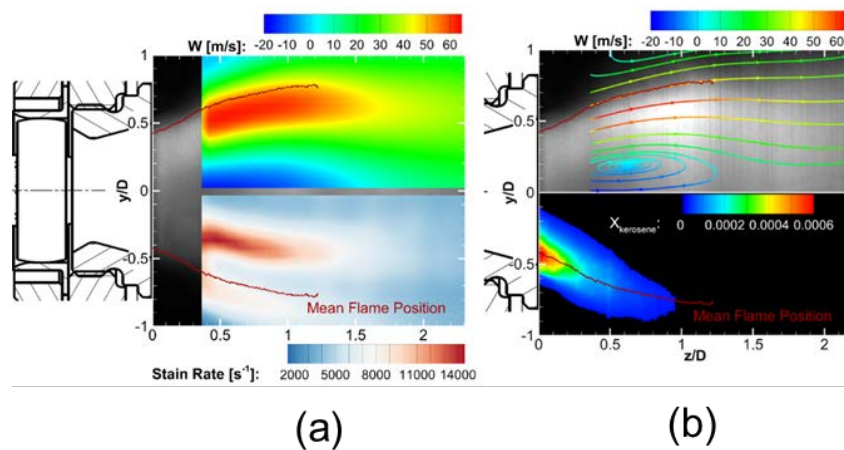
### 4.3 Fuel preparation and flame structure

Up to now, a detailed analysis was performed to study the effect of the four inlet droplet size distributions on the properties of the aerodynamics and the transportation of fuel droplets into the combustor. The objective is now to evaluate their effect on the fuel preparation and flame structure.

Experiments performed with the coupling of OH-PLIF and kerosene-PLIF diagnostics enabled us to give information on the interaction between the flame structure, the fuel/air mixture and the exhaust gases regions [14]. Results presented in Fig. 8a corresponds to the averaged 2D axial flow velocity on the top half side and the associated strain rate on the bottom half side while Fig. 8b displays the axial mean distributions of OH fluorescence signals (grey to white scale) and the streamlines determined from PIV measurements on the top half side while the bottom half side displays the kerosene vapor distribution (colour scale). Data are recorded at a pressure of 0.83 MPa. Furthermore, the flame position and flame length are also superimposed to both distributions (continuous line). The location of the mean flame, which



1 is representative of the reactive flame front is deduced from the calculation of the OH gradient  
 2 intensity from the instantaneous OH-PLIF images. First, the averaged concentration of vapor  
 3 kerosene remains low at the injector outlet with an average molar fraction close to  $5 \cdot 10^{-4}$ .  
 4 Considering the region in which kerosene vapor is detected, the measured equivalence ratio  
 5 would be  $\sim 0.05$  that prevents any chemical consumption of kerosene by combustion. The  
 6 measurements also indicate that the consumption of residual kerosene is still observed at the  
 7 interface between the zone of the fresh gases exiting from the injector and the exhaust gases.  
 8 The fact that the residual kerosene is consumed along this boundary results from the existence  
 9 of a large temperature gradient in the mixture layer located in the outside shear layer (OSL).  
 10 As the velocity gradient is large in OSL, its thickness is **small** and this one helps to a fast  
 11 preheating of the kerosene/air mixture to a temperature causing a reaction mechanism. This  
 12 result is supported by the analysis of joint instantaneous PLIF-OH and PLIF-kerosene images  
 13 which will be presented in Fig. 9. On the bottom side of Figs. 8a, it is also noted that the flame  
 14 is stabilized on the inner border of OSL. Indeed, vortices developing in OSL provide an  
 15 enhancement of the mixing between the kerosene/air mixture and hot gases coming from the  
 16 IRZ region. These favourable conditions then significantly increase the temperature of the  
 17 fresh gases in the mixing zone. Finally, it is also interesting to note that the distance for which  
 18 a reduction of velocity is observed in the jet zone coincides with the position of the end of the  
 19 flame length.  
 20  
 21  
 22  
 23  
 24  
 25  
 26  
 27  
 28  
 29  
 30  
 31  
 32  
 33  
 34  
 35  
 36  
 37  
 38  
 39  
 40  
 41  
 42  
 43  
 44  
 45  
 46  
 47  
 48  
 49  
 50  
 51  
 52  
 53  
 54  
 55  
 56  
 57  
 58  
 59  
 60  
 61  
 62  
 63  
 64  
 65



54 *Fig. 8: Averaged 2D axial flow velocity on the top half side and the associated strain rate on*  
 55 *the bottom half side (a); axial mean distribution of OH (grey to white scale) combined with*  
 56 *the streamlines on the top half side and kerosene vapor distribution on the bottom half side*  
 57 *(colour scale) (b).*

1 Effects of the pressure and the FAR on the modifications of the flame properties are also  
2 studied using OH-PLIF and kerosene-PLIF distributions. For instance, Fig. 9 shows the coupling  
3 between the axial and radial instantaneous distributions of OH fluorescence signals (grey to  
4 white scale) with the kerosene mole fraction (colour scale) on the top half side and with the  
5 temperature of the kerosene/air mixture on the bottom half side (colour scale), these ones  
6 being recorded for three operating conditions. Furthermore, the OH gradient intensity has  
7 been superimposed to visualize the intensity of the reaction zone (beige colour scale).  
8  
9

10  
11  
12  
13  
14 As observed in Fig. 9, the reactive flow at the exit of the injector looks like a “tulip” flame with  
15 high levels of OH mainly located along the flow axis and decreasing gradually into the  
16 combustion chamber. Kerosene vapor leaving the injection system is confined between IRZ  
17 and ORZ while the reaction zone is developing along the interface between these two regions.  
18  
19  
20  
21 Furthermore, the amount of kerosene mole fraction ejected from the injector is weak,  
22 indicating reaction mechanisms mostly taking place within the injection system itself.  
23  
24  
25 Increasing the pressure or reducing the FAR leads to a reduction in the quantity of fuel vapor  
26 as well as a reduction in the length of the fuel consumption area. These effects enhance the  
27 flame compactness and decrease the flame length. This change in flame structure arises from  
28 the modification in the pressure drop of kerosene across the fuel injector ( $\Delta P$ ) which changes  
29 significantly when pressure increases:  $\Delta P=0.73$  MPa for  $P=0.83$  MPa,  $\Delta P=1.27$  MPa for  $P=1.38$   
30 MPa and  $\Delta P=1.53$  MPa for  $P=1.8$  MPa. An increase of the pressure drop then increases the  
31 atomization of the liquid jets, leads to a faster evaporation and finally favours the  
32 consumption of kerosene inside the injection system bowl. This effect is confirmed by the  
33 observation of a significant reduction of the intensity of the OH gradient along the flow axis.  
34  
35  
36  
37  
38  
39  
40  
41  
42  
43

44 These results are corroborated by the radial distributions of OH and kerosene measured in the  
45 plane located at  $Z/D = 0.75$ . As mentioned above, the region of burned gases is reduced in size  
46 while the OH fluorescence decreases when the pressure increases. The quantity of fuel vapor  
47 detected becomes residual (around 100 ppm) while the fresh gases increase in temperature.  
48  
49  
50  
51 These observations therefore support the idea that an increase in pressure leads to a better  
52 combustion inside the injection system bowl leading to a reduction at the outlet of the  
53 injection system of the reaction zone. Once the kerosene is consumed and the reaction zone  
54 is no longer observed, the production of OH is stopped and its mole fraction is gradually  
55 reduced when it is transported downstream of the injector. As the acceleration zone of the  
56  
57  
58  
59  
60  
61  
62  
63  
64  
65

burnt gases resulting from thermal expansion disappears at the end of the reaction zone, the temperature of the burnt gases at this position seems to decrease due to the mixing of the hot gases with the gases located at the periphery of the flame.

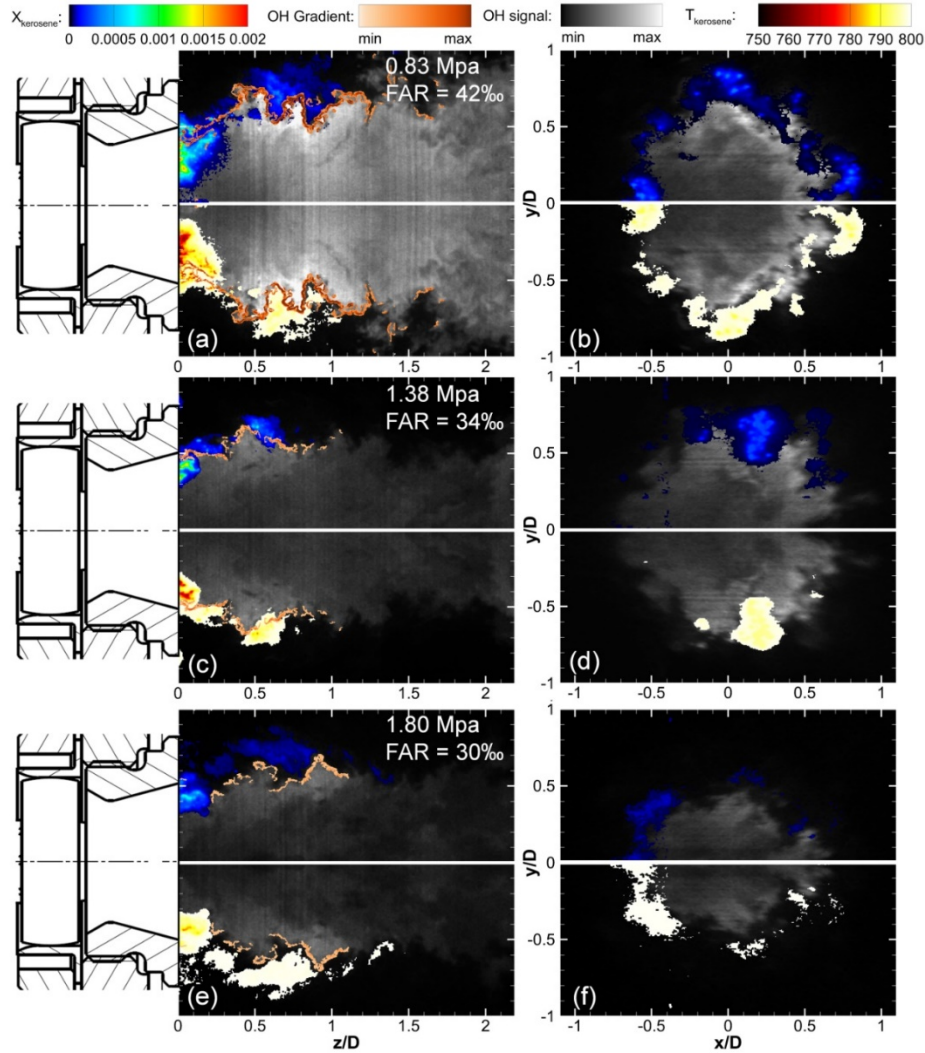


Fig. 9: Single-shot axial (left) and radial at  $Z/D = 0.75$  (right) distributions of kerosene mole fraction and OH radical for three operating conditions.  $P=0.83$  MPa,  $FAR=42\%$  (top),  $P=1.38$  MPa,  $FAR=34\%$  (middle) and  $P=1.8$  MPa,  $FAR=30\%$  (bottom).

In order to support these experimental results, numerical simulations were performed to calculate the kerosene vapor and OH distributions for the different inlet droplet size distributions. Regarding the prediction of the instantaneous axial distributions of kerosene vapor shown in Fig. 10, the numerical kerosene vapor spatial distribution reproduces similar spotty patterns like the experimental ones excepted may be for the  $D_1$  case in which a large

1 zone of kerosene ~~is developing~~ at the exit of the injection system. Concerning the time-  
2 averaged distributions, the kerosene vapor distribution calculated with the  $D_1$  droplet  
3 distribution spreads over a large distance in the combustion chamber as opposed to the  
4 experimental case. This theoretical evolution is consistent with the fact that the fuel droplets  
5 are transported farther downstream from the injection system delaying then their fast  
6 evaporation. The  $D_2$  droplet distribution also produces a kerosene vapor distribution  
7 spreading farther downstream but with a narrower and shorter growth. Regarding now the  
8  $D_3$  and  $D_4$  distributions, the numerical results are very close to the experimental results. On  
9 the one hand, the kerosene vapor distribution for the  $D_3$  droplet distribution extends on the  
10 same length than the experimental one. On the other hand, the  $D_4$  droplet distribution  
11 produces a kerosene vapor distribution slightly reduced in size but traces of kerosene are still  
12 observed farther downstream. Instantaneous and time-averaged OH molar fractions  
13 displayed in Fig. 11 are now compared with the experimental OH-PLIF measurements. As  
14 stated before, the  $D_1$  droplet size distribution leads to a large spatial distribution of droplets  
15 along the jet flow. This droplet pattern generates a reaction zone fully detached, leading to  
16 the production of a V-shape flame as opposed to the experimental one. On the other hand,  
17 the  $D_2$  to  $D_4$  droplet distributions well capture the tulip-shape flame topology. The  
18 instantaneous OH distributions also reproduce the branched experimental profile of the  
19 flame, while the time-averaged distributions simulate the width of the flame. These results  
20 are important to consider for the future. Indeed, unlike kerosene-PLIF, PDA and PIV  
21 measurements, OH-PLIF measurements are relatively insensitive to the inlet droplet size  
22 distributions which can be an important constraint for the validation of numerical predictions  
23 of two-phase flow combustion when only these measurements are used .  
24  
25  
26  
27  
28  
29  
30  
31  
32  
33  
34  
35  
36  
37  
38  
39  
40  
41  
42  
43  
44  
45  
46  
47  
48  
49  
50  
51  
52  
53  
54  
55  
56  
57  
58  
59  
60  
61  
62  
63  
64  
65

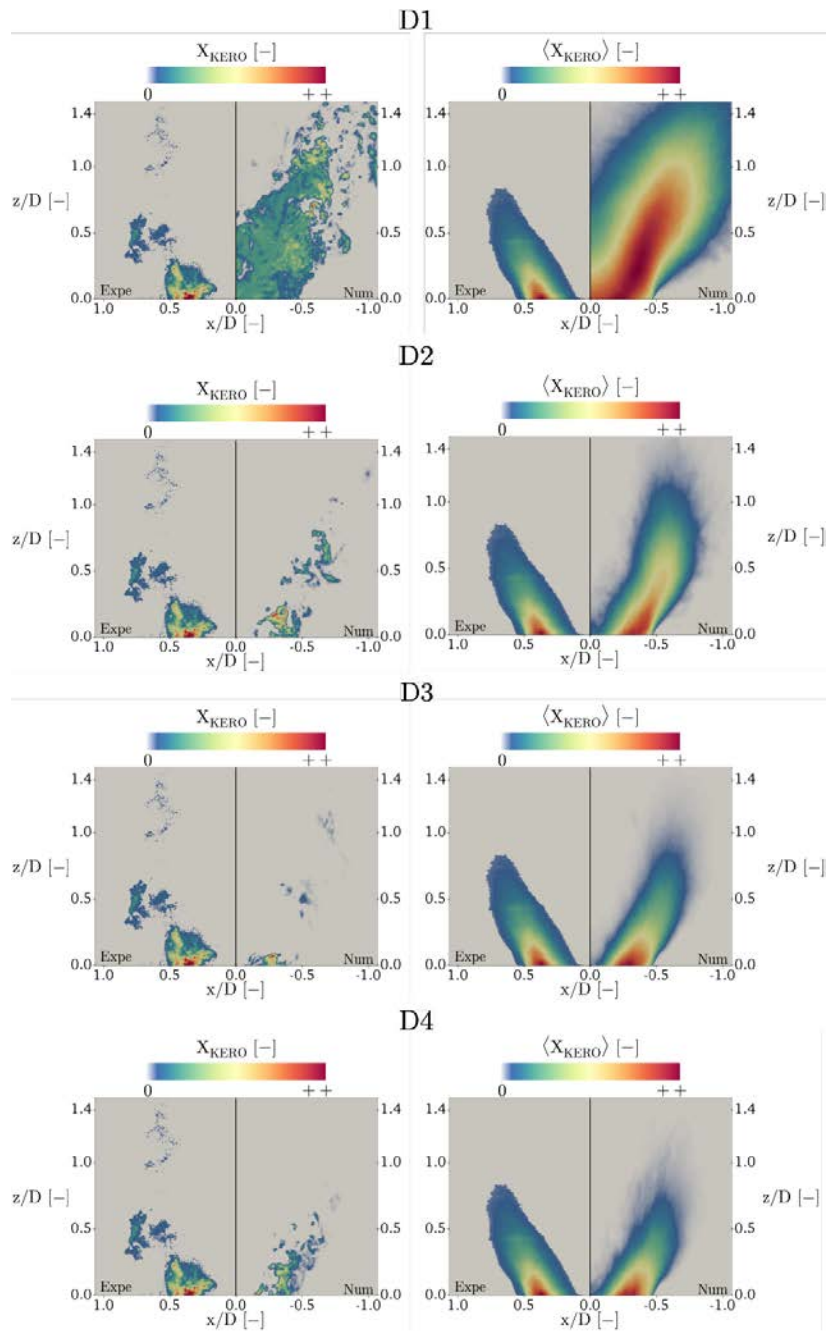

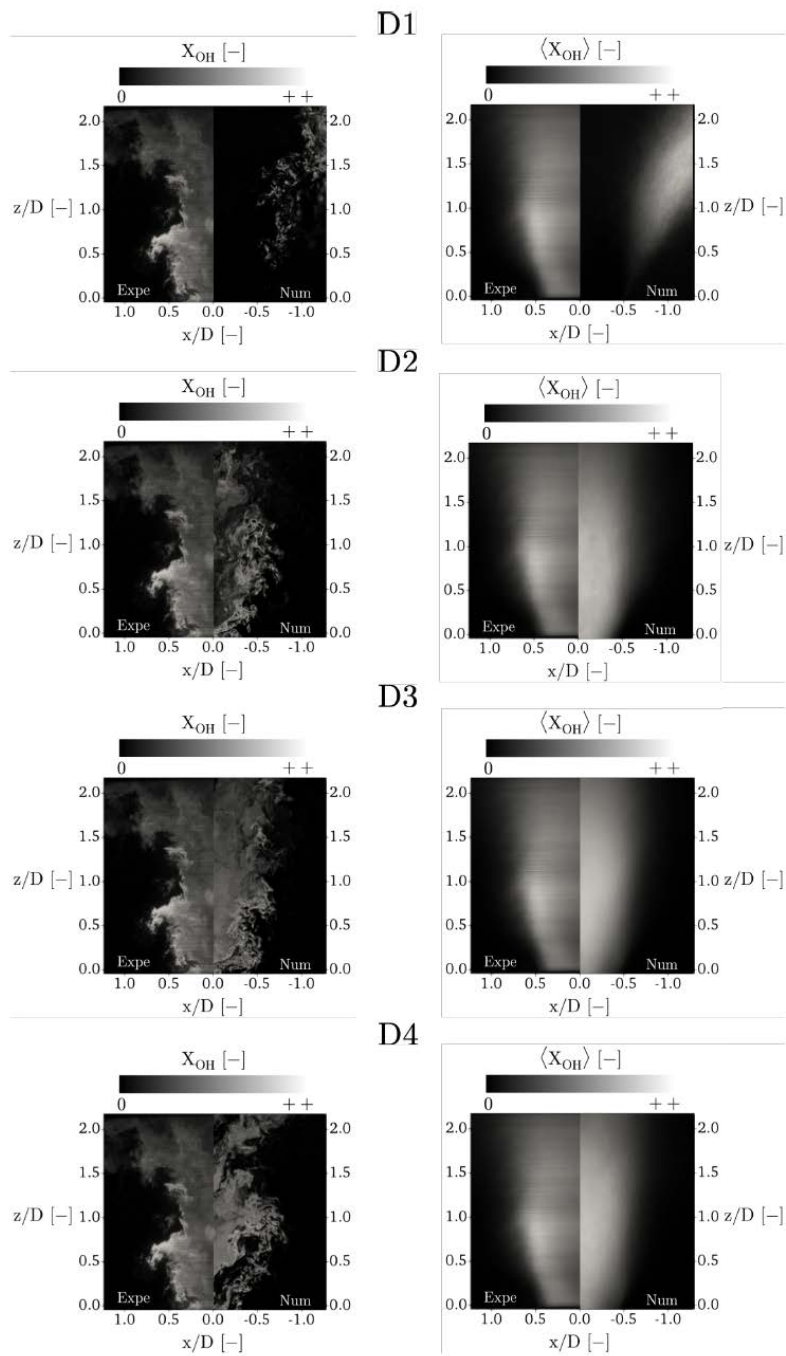


Fig. 10: Axial comparison of instantaneous (left) and time-averaged (right) kerosene vapor distribution between the numerical experimental results 

1  
2  
3  
4  
5  
6  
7  
8  
9  
10  
11  
12  
13  
14  
15  
16  
17  
18  
19  
20  
21  
22  
23  
24  
25  
26  
27  
28  
29  
30  
31  
32  
33  
34  
35  
36  
37  
38  
39  
40  
41  
42  
43  
44  
45  
46  
47  
48  
49  
50  
51  
52  
53  
54  
55  
56  
57  
58  
59  
60  
61  
62  
63  
64  
65

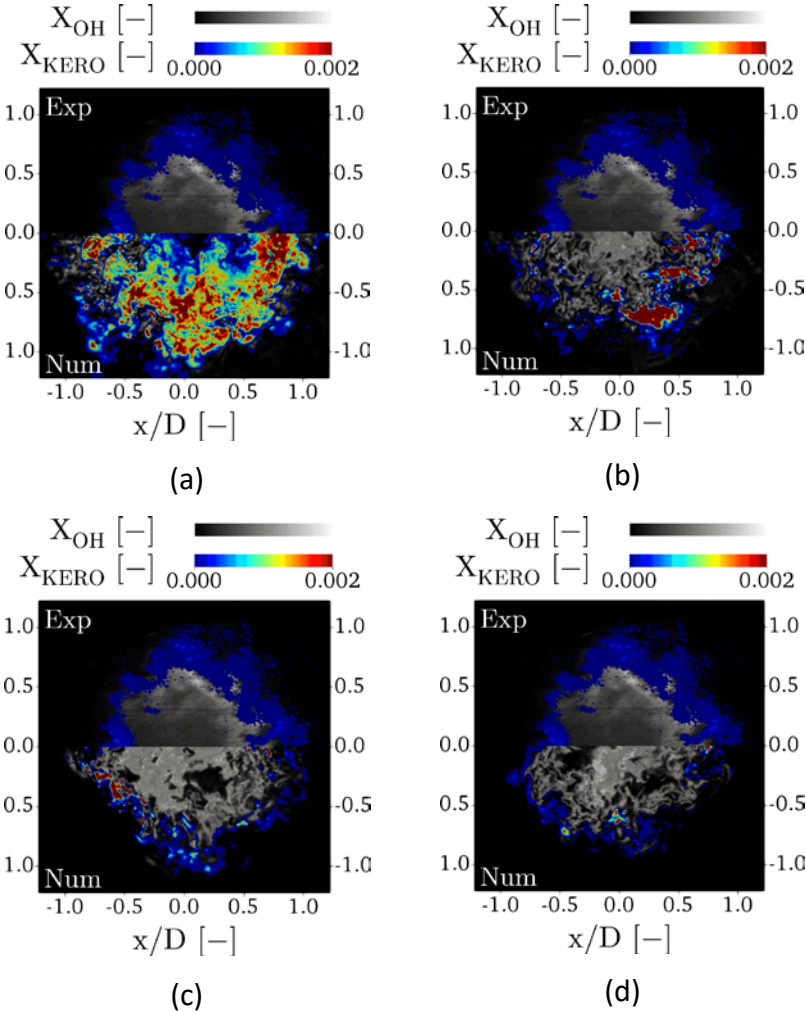


*Fig.11: Axial comparison of instantaneous (left) and time-averaged (right) OH distribution between numerical and experimental results*

Finally, the radial views of the kerosene vapor and OH instantaneous molar fractions distributions recorded at  $Z/D = 0.75$  are presented together with the numerical predictions in Fig. 12. The upper part of each picture corresponds to the experimental results while the lower part represents the numerical results. First, the  $D_1$  droplet size distribution generates



1 misplaced distributions while the flame is spreading over a larger region than the experimental  
 2 one. This result is somewhat expected in regards to the simulated V-shape flame topology.  
 3  
 4 Second, the simulated kerosene vapor concentration differs both in terms of absolute values  
 5 and radial distributions. Results obtained with the  $D_2$  droplet distribution shows a better  
 6 agreement with the experimental results. However, the flame is a little wider and the  
 7 concentration of kerosene vapor continues to be overpredicted. Finally, the  $D_3$  and  $D_4$  droplet  
 8 distributions predict comparable thicknesses for the OH and kerosene vapor spatial  
 9 distributions like those recorded during the experiments.  
 10  
 11  
 12  
 13  
 14  
 15



50 *Fig.12: Radial plane comparison between the experimental (top) and numerical (bottom)*  
 51 *instantaneous kerosene vapor and OH distributions at  $z=D = 0.95$  for the*  
 52 *distribution  $D_1$  (a),  $D_2$  (b),  $D_3$  (c) and  $D_4$  (d).*  
 53  
 54  
 55  
 56  
 57  
 58  
 59  
 60  
 61  
 62  
 63  
 64  
 65

#### 4.4 NO production

To quantitatively measure NO concentration while avoiding interference with the kerosene fluorescence, the simultaneous detection of both species is imperative. Indeed, aromatics naturally present in the kerosene chemical composition absorb part of the laser beam at 226 nm and re-emits photons by fluorescence in the spectral domain in which NO fluorescence is detected. For instance, Fig. 13 shows the single-shot distributions of raw-NO-PLIF, kerosene-PLIF and NO-PLIF masked from the kerosene-PLIF signal recorded simultaneously.

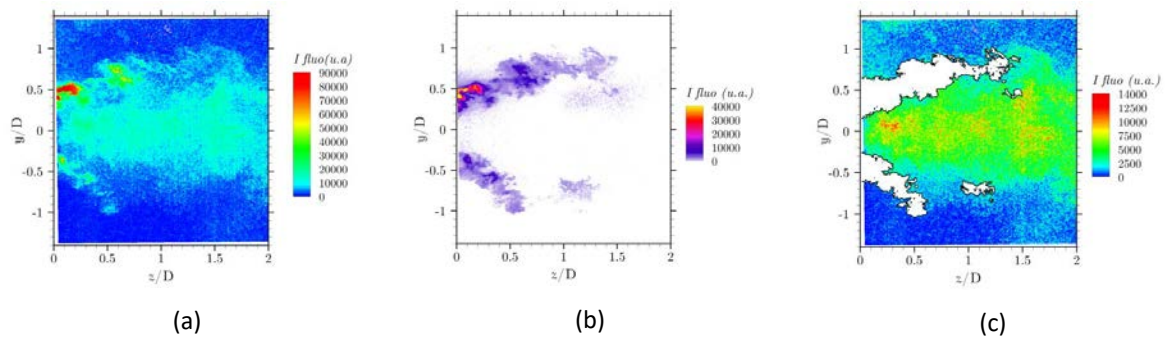


Fig. 13: Simultaneous single-shot raw NO-PLIF (a), kerosene-PLIF (b) and NO-PLIF masked from the kerosene-PLIF signal (c).  $P=0.83$  MPa, FAR= 42 % and inlet  $T_{air} = 670$  K.

A comparison between the images displayed in Figs 13a and 13b clearly shows that the shape of the kerosene fluorescence signal displayed in Fig. 13b is also discernible on the raw NO fluorescence image (Fig. 13a). This result leads to a partial overlap between kerosene fluorescence signals and NO fluorescence signals. Hopefully, no kerosene fluorescence is observed in the major part of the NO fluorescence image, that supports a possible analysis of the NO fluorescence signals in terms of mole fraction measurements. To process the NO fluorescence images, the kerosene fluorescence region is first isolated from the NO fluorescence by means of a nonlinear diffusive filter. This procedure makes it possible not only to preserve the contours of the kerosene vapor pockets but also to make the thresholding less sensitive to noise. The frontiers delimiting the kerosene pockets are then obtained by thresholding these filtered images. The resultant images are finally served to the definition of a binary mask, this one being applied to the raw NO fluorescence images. As a result, the white areas on the NO fluorescence images observed in Fig. 13c thus correspond to the kerosene fluorescence region that has been masked.



After a conversion phase of the NO fluorescence signals in NO mole fraction by the procedure developed and detailed in [15], Fig. 14a shows the mean NO concentration spatial distribution over which the streamlines are superimposed. First of all, it is noted that the dark areas in the outer shear layer do not correspond to an absence of NO. Indeed, the detection of kerosene fluorescence signals in this zone prevents any measurement of NO concentration because both fluorescence signals are spatially superimposed. In the lower left corner, the NO mole fraction values are also not representative of real NO concentration values. Due to the absorption of the laser sheet by kerosene in the area of few millimetres thick located just at the outlet of the injector, the energy in the laser sheet becomes so attenuated that it is impossible to correctly convert the fluorescence signal into NO concentration. As a result, the molar fraction distribution measured in this area is greatly underestimated.

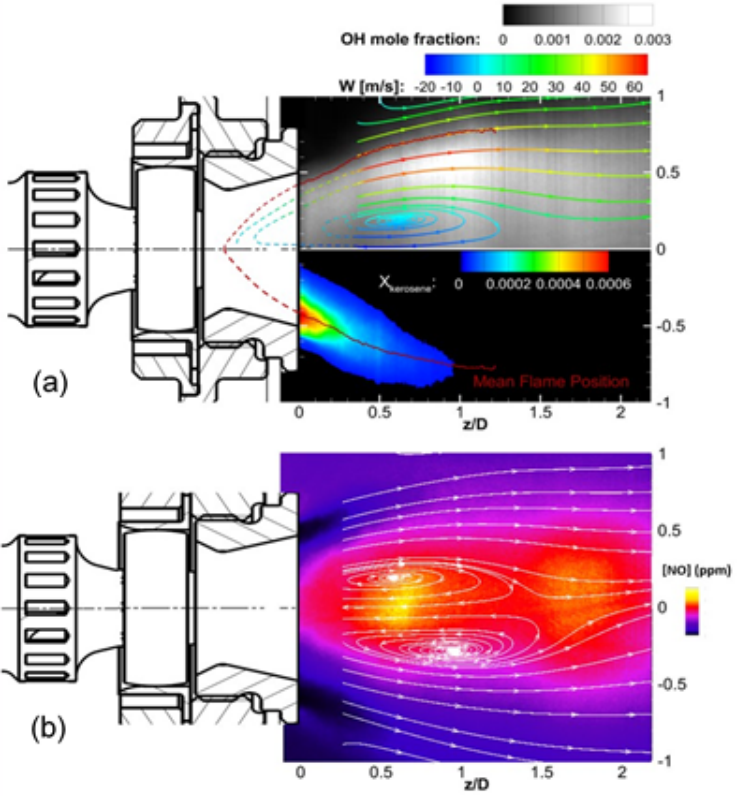


Fig. 14: Averaged axial distribution of OH and kerosene vapor mole fraction (a) and NO mole fraction (b) at  $P=0.83$  MPa. The streamlines are superimposed on both images.

In the exploitable areas of Fig. 14a, two zones of high levels of NO molar fraction are easily discernible. The first NO pocket ( $\sim 500 - 650$  ppm) is located at the exit of the injection system outlet while the second one with an equivalent amount of NO concentration ( $\sim 400 - 600$

1 ppm) follows the first NO pocket. To explain the physical reasons of these two specific NO  
2 pockets, an observation of the streamlines shown in Fig. 14a reveals that the first NO pocket  
3 is located into IRZ, a region where high-temperature exhaust gases recirculate (see Fig. 14b).  
4 Furthermore, the gas velocities in IRZ are so weak that the residence time of NO becomes  
5 significant which favours the subsistence of this pollutant by the NO thermal mechanism. The  
6 second region delivering a high level of NO is located right after closing IRZ. One plausible  
7 explanation of the overproduction of NO may originate from the mutual interaction of the  
8 thermal and nitrous oxide pathways [30]. Indeed, N<sub>2</sub>O is a chemical intermediate which has a  
9 very short lifetime. It is commonly produced in the flame front through chemical reactions  
10 involving H radicals or CO molecules and almost fully transformed in NO in the combustion  
11 products under the attack of free radicals. In the current study, following the streamlines, NO  
12 can be produced as a result of the rapid transportation of N<sub>2</sub>O from ISL, where it is initially  
13 produced, to the hot central region downstream IRZ. Under the action of high velocities, the  
14 residence time of N<sub>2</sub>O will be reduced, which will then favour in combination with a high level  
15 of temperature the NO production by a conversion of N<sub>2</sub>O via the N<sub>2</sub>O chemical mechanism.  
16 Remember also that the NO production by the destruction of N<sub>2</sub>O is also particularly effective  
17 at high pressure, which is the case in the current study.  
18  
19  
20  
21  
22  
23  
24  
25  
26  
27  
28  
29  
30  
31  
32

33 Figure 15 shows the evolution of the distribution of the mole fraction of NO as a function of  
34 the pressure and the FAR. Results presented in Fig. 15 reveal an increase of the mole fraction  
35 with pressure. For the operating conditions tested, a significant amount of NO is located in  
36 the IRZ recirculation zone. This amount of NO comes mainly from combustion inside the bowl  
37 of the injection system. In contrast, the second maximum zone of NO downstream of IRZ  
38 increases with FAR. By analysing the velocity fields recorded under the different pressures  
39 tested, no significant change of the aerodynamic flow pattern is observed, which seems to  
40 indicate an insensitivity of the NO production with this parameter. Similarly, the mole fraction  
41 of NO increases significantly with FAR. This result can be explained by an increase of the  
42 combustion temperature and consequently that of the hot gases circulating in IRZ  
43  
44  
45  
46  
47  
48  
49  
50  
51  
52  
53  
54  
55  
56  
57  
58  
59  
60  
61  
62  
63  
64  
65

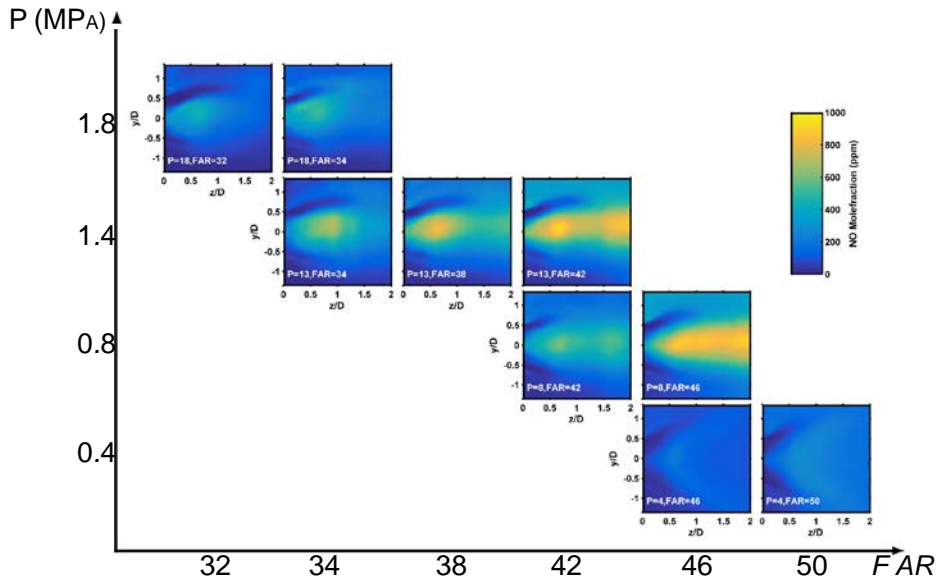
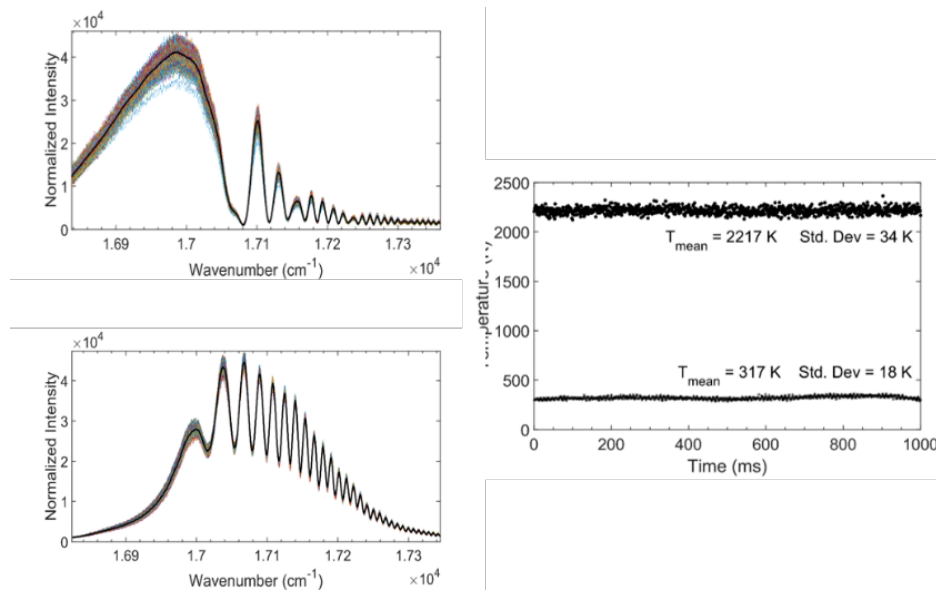


Fig. 15: Effect of pressure and FAR on the time-averaged NO spatial distributions

#### 4.5 Temperature measurements

The CPP fs-CARS diagnostic in the current study has been specifically developed to perform temperature measurements at high repetition rates in high-pressure reactive flows. The CARS spectra were analysed using an in-house written software. The first step was to subtract background emission from the CARS spectrum. The background emission was either collected in the emCCD camera when no CARS signal was created. The experimental CARS spectra were then compared to numerical simulations using a "Differential Evolution" algorithm [24] which aims at minimizing by a least-squared method, the difference between the single-shot CARS spectrum and the theoretical spectrum presenting the best agreement. An iterative procedure is then set up to identify the optimal set of parameters presenting the best minimization between the experimental and theoretical spectrum. In this procedure, the parameters to be adjusted by the genetic algorithm are twelve: the 2<sup>nd</sup> and 3<sup>rd</sup> order spectral phase parameters of the Pump, Stokes and probe laser beams, the relative delays between laser pulses, the ratio  $\beta/\alpha$  and the phase shift  $\varphi$  between the resonant and non-resonant contributions, the frequency shift on the camera, as well as the temperature. These parameters are determined by the analysis of a reference CARS spectrum recorded in a N<sub>2</sub> jet at known temperature. An application of the genetic algorithm then makes it possible to determine all the unknown parameters, except the temperature, which is already known. Once these parameters have

1 been determined, the CARS spectra recorded at other thermodynamics conditions are  
 2 analysed by leaving now the temperature parameter free and setting the other adjustment  
 3 variables around the reference values. To validate this procedure of processing of the CARS  
 4 spectra, single fs CARS spectra of  $N_2$  were first recorded in an air jet heated at  $45^\circ C$ , then in a  
 5 stoichiometric laminar premixed  $CH_4$ -air flame. An example of results obtained during these  
 6 experiments is depicted on Fig. 16. For each condition, the mean experimental spectra are  
 7 superimposed to 1000 single-shot CARS spectra. First, it is remarkable to note the  
 8 reproducibility of the single-shot CARS spectra which is mainly related to the good temporal  
 9 stability of the laser energy pulses emitted by the femtosecond laser system. Thus, these  
 10 conditions allow to measure the mean temperature and rms temperature fluctuations and an  
 11 accuracy of 6 % at 317 K and 1.5 % at 2240 K are obtained.



12  
 13  
 14  
 15  
 16  
 17  
 18  
 19  
 20  
 21  
 22  
 23  
 24  
 25  
 26  
 27  
 28  
 29  
 30  
 31  
 32  
 33  
 34  
 35  
 36  
 37  
 38  
 39  
 40  
 41  
 42  
 43  
 44  
 45  
 46  
 47  
 48  
 49  
 50  
 51  
 52  
 53  
 54  
 55  
 56  
 57  
 58  
 59  
 60  
 61  
 62  
 63  
 64  
 65

Fig.16: 1000 instantaneous and the resultant averaged CPP fs-CARS spectra recorded at 1 kHz in a heated air flow and a  $CH_4$ /air premixed flame (left) and associated time history profiles of single-shot temperature measurements (right).

Then, CPP fs-CARS spectra were then recorded in the HERON facility in which a multi-point Low-NOx injection system fed with liquid kerosene (Jet A1) was tested. The injection system is composed of a single pilot injector located on the combustor axis and it is used to stabilise the flame whereas a multipoint main injector is located at larger radial distance. Fuel flowrate is split between the two injectors and the ratio between equivalence ratio from the pilot and the main injector ( $\Phi_{pilot}/\Phi_{main}$ ) lies between 0.1 and 1, except for a condition where only

the pilot injector is used. The operating conditions in which CARS measurements were performed are resumed in Table 2.

	Air inlet temperature (K)	Pressure (MPa)	$\Phi_{\text{pilot}}/\Phi_{\text{main}}$	Global equivalence ratio
Case 1	720	0.75	0.22	0.59
Case 2	720	0.75	0.26	0.55

*Table 2: Operating conditions for CPP fs-CARS measurements in high-pressure flames*

Figure 17 shows the time evolution of temperature measurements from 1000 sequential single laser shots recorded in the region of burnt gases located just behind the Inner recirculation zone ( $Z/D=1.5$ ). Results correspond to case 1 and they are recorded at a frequency rate of 1 kHz. Each data point represents a temperature measurement from the data processing of a single-shot CARS spectrum. Also included in Fig. 17 are typical single-shot CARS spectra recorded at various times at the same probe volume location. For each spectrum, the experimental spectrum is presented along with the best-fit theoretical CARS spectrum. Although the levels of turbulence and temperature in the combustion chamber are not negligible at this probe volume position, their effect on the propagation of the laser beams remains small, which allows to keep efficient beam crossings and to have a very accordance between the CARS spectra and finally, a good confidence on the resultant temperature measurements.

To analyse the sensitivity of the CARS thermometry in high-pressure kerosene/air flames, CARS experiments were also performed for two different conditions of equivalence ratio. Note in this experiment that the variation of the equivalence ratio is deliberately small in order to be able to quantify the performances of the CPP fs-CARS in capturing small temperature variations. As an example of results, Fig. 18 shows the time history plots of temperature measurements recorded during 1 sec for cases 1 and 2 at the same probe volume location. For both cases, the time history profiles reveal large and fast variations of temperature for 0.01 to 0.1 s in time. These variations, which are easily discernible with the CPP fs-CARS diagnostic, are the result of intense mixing taking place between the burnt gases produced by the flame and heated inlet air circulating around the periphery of the flame. As explained previously, the origin of this air flow is only related to the operation of the combustion chamber which requires for reasons of thermal resistance, an injection of air along the walls

of the combustion chamber. Finally, the right-hand side of Fig. 18 shows the associated probability density function (Pdf) in which the Gaussian envelope is also included. The Pdf are built with a temperature column step of 40 K matching the uncertainty of CARS measurements in stationary conditions. The scatter in the results, larger than the CARS measurement uncertainty, gives insight into the degree of turbulence of the reactive flow. A comparison of both Pdfs also shows the capacity of the CPP fs CARS to capture a decrease of the mean temperature when the global equivalence ratio is decreasing while the scale of the rms of temperature fluctuations are of the same order of magnitude.

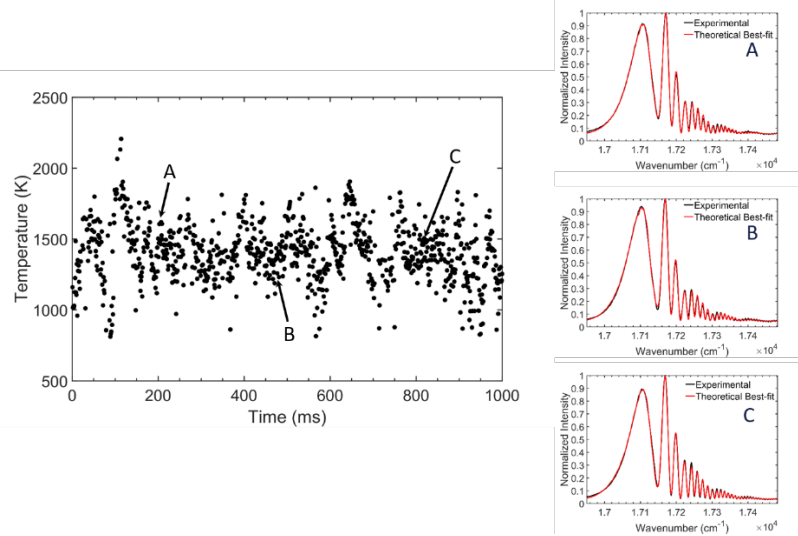


Fig. 17: Time history profile of 1000 sequential single-shot temperature measurements (left) and various comparisons of experimental spectrum with theoretical fit for laser shot number A, B and C. Operating conditions:  $P=0.75$  MPa, global equivalence ratio = 0.59.

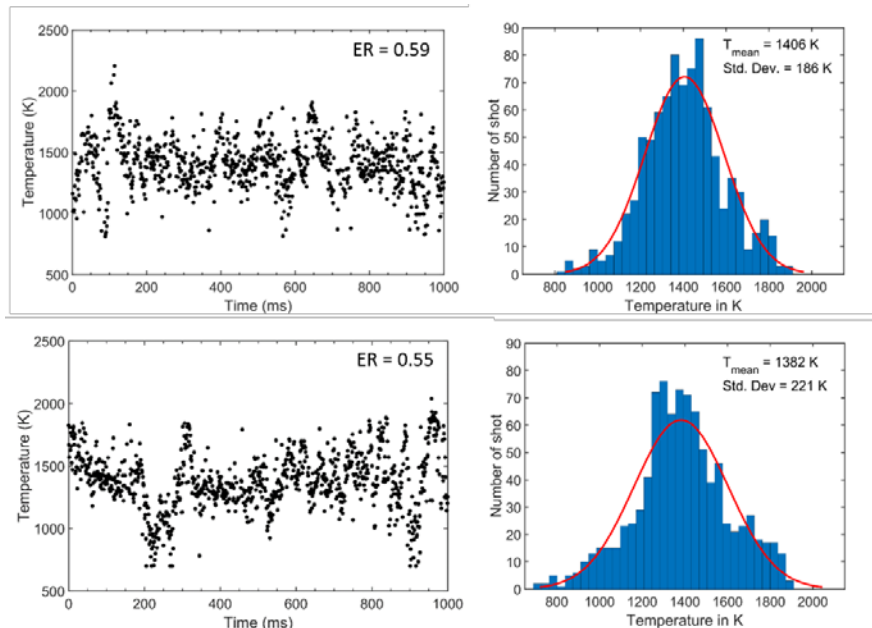


Fig. 18: Time history profiles of 1000 sequential single-shot temperature measurements (left) and associated histograms (right) recorded for two global equivalence ratios.

## 5. Conclusions

A gas turbine model combustor equipped with an innovative lean premixed fuel injection system provided by SAFRAN Helicopter Engines and supplied by liquid kerosene was experimentally investigated to study the effect of pressure on the flame properties and NO formation. Various laser-based diagnostics such as PIV, PDA, OH-PLIF, kerosene-PLIF, and NO-PLIF were used both individually or in combination for custom-made solutions able to access to useful data on the spatial distributions of velocity, droplets size, OH, kerosene and NO molar fractions. Measurements were performed for various conditions of pressure ranging from 0.4 to 1.8 MPa and for different FAR representative of the ones encountered in real aeronautic propulsion systems. For pressures larger than 0.4 MPa, the mean velocity and the flame shape distributions are typical of enclosed swirled flames forming a tulip-shape flame with the production of an inner recirculation zone and an outer recirculation zone. The position and structure of the reaction zone were identified using OH-PLIF. Reaction zones were formed at the outer of inner shear layers where the hot gases mix with the kerosene/air mixture issued from the injection system. A detailed analysis of velocity and OH distributions also shows that the flame is stabilized inside the injection system bowl thanks to the presence of a large inner recirculation zone and to a fast evaporation of the kerosene droplets. Complementary single-shot measurements of NO distributions were also conducted by NO-PLIF with an excitation

1 wavelength near to 226 nm. The measurement strategy adopted in the current study to  
2 measure NO distribution enables an isolation of NO fluorescence signals from interferences  
3 causing from kerosene fluorescence. It is then observed that NO formation is governed by the  
4 Zeldovich and nitrous oxide pathways depending on the positions in the flame. NO is  
5 preferentially formed by the thermal mechanism in IRZ while a second peak of NO observed  
6 right behind IRZ is presumably governed by the nitrous oxide mechanism. Results of NO  
7 measurements also show that the conditions of pressure and FAR inside the combustor play  
8 an important role in the development of the NOX emission pathways.  
9

10  
11  
12  
13  
14  
15  
16 In parallel to this experimental study, Large-Eddy simulations of the current flame was  
17 performed using the PCM-FPI tabulated chemistry approach. The two-phase flow was  
18 calculated by a polydisperse Euler-Lagrangian approach. Specifically, a numerical parametric  
19 study with various inlet fuel droplet size distributions injected at the exit of the injector was  
20 performed to quantify the effect of the spray properties on the flame properties. Only one  
21 experimental operating condition of pressure and FAR was used in these simulations. First of  
22 all, LES results were compared to the experimental flow data in terms of mean and  
23 fluctuations of axial and radial velocity as well as droplet diameter distributions. The topology  
24 of the velocity field characteristic of a swirl flow with a large ORZ along the flow axis, was  
25 reproduced numerically when using the  $D_3$  inlet droplet size distribution. Large differences in  
26 behaviour are observed for the other inlet droplet size distributions indicating a preponderant  
27 role of the inlet spray properties in terms of droplet size on aerodynamics. This is supported  
28 by the comparison of the measured and calculated droplet size distributions downstream  
29 from the injector exit, which clearly demonstrates the impact of the inlet spray injection  
30 conditions on the distribution of the size of droplets ejected from the injection system.  
31 Complementary comparisons between the predictions of the kerosene vapor and OH spatial  
32 distributions and the experimental data endorse this result. Evaporated kerosene distribution  
33 at the same locations than those probed with PDA shows the same trends, i.e. a better  
34 concordance between measurements and numerical calculations for the  $D_3$  droplet size  
35 distribution. The OH distributions are also well predicted except for the  $D_1$  droplet distribution  
36 in which large droplets in size guide the flame front along the jet flow.  
37  
38  
39  
40  
41  
42  
43  
44  
45  
46  
47  
48  
49  
50  
51  
52  
53  
54  
55

56  
57 Further work will focus on novel laser diagnostics, especially to measure the temperature  
58 distribution in the flow field. These results are necessary for the optimization of the new  
59  
60  
61  
62  
63  
64  
65



1 generation of Low-NO<sub>x</sub> injection systems, but also to obtain a better understanding of the  
2 quantification of NO pollutant inside the combustion as well as for the development and  
3 validation of numerical models aiming to accurately simulate turbulent high-pressure  
4 kerosene/air flames. To this end, a demonstration of the application of the CPP-fs CARS  
5 diagnostic for single-shot temperature measurements on high-pressure kerosene/air flames  
6 was shown. Measurements were recorded on an innovative multi-point injection system  
7 running at 0.8 MPa. The repetition rate of single-shot temperature measurements was fixed  
8 to 1 kHz and the flame was explored on various axial and radial locations. The CARS spectra  
9 were data processed using a genetic algorithm based spectral fitting solver. Results carried  
10 out in high-pressure operating conditions emphasize the potential of CPP fs CARS to acquire  
11 time series of temperature data in a fraction of measurement time compared to conventional  
12 10 Hz point measurements. In addition to the opportunities offered to study dynamic  
13 phenomena in the next future, the drastic reduction of time measurements will be an essential  
14 step towards a significant reduction of operating costs of high-pressure gas turbine model  
15 combustors.

## 30 **6. Acknowledgements**

31 The authors are grateful for the financial support of the French aircraft motorist SAFRAN and  
32 the French National Research Agency (Industrial Chair PERCEVAL ANR-15-CHIN-0001). We also  
33 thank B. Quevreux and F. Frindt for their technical support.

## 38 **References**

- 39 [1] A. Valdés, R.M. Burmaoglu, S. Tucci, V. Braga da Costa, L.M. Campos, L. Mattera, V.F.  
40 Gomez Comendador, Flight Path 2050 and ACARE Goals for Maintaining and Extending  
41 Industrial Leadership in Aviation: A Map of the Aviation Technology Space. Sustainability, 11(7)  
42 (2019) 2065-2089.
- 43 [2] T.C. Lieuwen, V. Yang, Gas Turbine Emissions, Cambridge University Press, 2013.
- 44 [3] A.H. Lefevre, D.R. Ballal, Gas Turbine Combustion: alternative fuels and emissions in Third  
45 Edition, Taylor & Francis, 2010.
- 46 [4] J. Janicka, A. Sadiki, M. Schäfer, C. Heeger, Flow and Combustion in Advanced Gas Turbine  
47 Combustors, Springer Dordrecht Heidelberg New York London, 2013.

1 [5] S.M. Correa a review of NO<sub>x</sub> formation under gas turbine combustion conditions, Comb.  
2 Sci. technol. 87 (1993) 239-362  
3

4 [6] F. Grisch, M. Cazalens, Prepare for the Future Making Aero Engine Clean and Efficient,  
5 Impact, Science Impact Ltd, vol. 2016, Number 2, (2016), 52-54  
6

7 [7] F. Grisch, A. Boukhalfa, G. Cabot, B. Renou, A. Vandiel, CORIA Aeronautical combustion  
8 facilities and associated optical diagnostics, Aerospace Lab Journal, Issue 11 (2016).  
9

10 [8] P. Malbois, E. Salaun, F. Frindt, L. Bouheraoua, H. Verdier, S. Richard, G. Cabot, B. Renou,  
11 F. Grisch Experimental Investigation on the Performances of a Lean-Premixed Aero-engine  
12 Injection system Under Relevant Operating Conditions, ASME Turbo Expo 2017 – Charlotte  
13 (USA), GT2017-64484 (2017).  
14  
15

16 [9] V. Moureau, P. Domingo, L. Vervisch - From Large-Eddy Simulation to Direct Numerical  
17 Simulation of a Lean Premixed Swirl Flame: Filtered Laminar Flame-PDF Modeling, Combust.  
18 Flame 158 (7) (2011) 1340–1357.  
19  
20

21 [10] M. Malandain, N. Maheu, V. Moureau - Optimization of the Deflated Conjugate Gradient  
22 Algorithm for the Solving of Elliptic Equations on Massively Parallel Machines. J. Comput. Phys.  
23 238 (2013) 32–47.  
24  
25

26 [11] B. Ofner, Phase Doppler Anemometry (PDA). In: Mayinger F., Feldmann O. (eds) Optical  
27 Measurements. Heat and Mass Transfer. Springer, Berlin, Heidelberg, 2001.  
28  
29

30 [12] H.E. Albrecht, M. Borys, N. Damaschke, C. Tropea, Laser Doppler and Phase Doppler  
31 Measurement Techniques, Springer, Heidelberg, 2003.  
32  
33

34 [13] A. Schröder, C. Willert, Particle Image Velocimetry "New Developments and Recent  
35 Applications", Topics in applied physics 112, Springer Berlin, Heidelberg, New York, 2008  
36  
37

38 [14] P. Malbois, E. Salaün, B. Rossow, G. Cabot, L. Bouheraoua, S. Richard, B. Renou, F. Grisch,  
39 Quantitative measurements of fuel distribution and flame structure in a lean-premixed aero-  
40 engine injection system by kerosene/OH-PLIF measurements under high-pressure conditions,  
41 Proceedings of the Combustion Institute, 37 (2019) 5215-5222.  
42  
43

44 [15] E. Salaun, F. Frindt, G. Cabot, B. Renou, S. Richard, M. cazalens, P. Malbois, F. Grisch,  
45 Experimental Investigation on NO Pollutant Formation in High-Pressure Swirl-Stabilized  
46  
47  
48  
49  
50  
51  
52  
53  
54  
55  
56  
57  
58  
59  
60  
61  
62  
63  
64  
65

1 Kerosene/air Flames Using NO-, OH- and Kerosene-PLIF and and PIV Laser Diagnostics - ASME  
2 Turbo Expo 2020 – London (UK), GT2020-14985 (2020).

3  
4 [16] A.C. Eckbreth, Laser Diagnostics for Combustion Temperature and Species (Gordon and  
5 Breach, Amsterdam, 1996.

6  
7  
8  
9 [17] S.A. Druet, J.P. Taran, CARS Spectroscopy, Progress in Quantum Electronics, 7 (1981) 1-  
10 72.

11  
12 [18] F. Grisch, Coherent anti-Stokes Raman scattering (CARS) in Combustion, Laser Diagnostics  
13 in Combustion, Edited by M. Lackner, Verlag ProcessEng Engineering GmbH (2009).

14  
15  
16  
17 [19] S. Roy, J.R. Gord, A.K. Patnaik, Recent advances in coherent anti-Stokes Raman scattering  
18 spectroscopy: Fundamental developments and applications in reacting flows, Progress in  
19 Energy and Combustion Science, 36 (2010) 280-306.

20  
21  
22 [20] D.R. Richardson, R.P. Lucht, W.D. Kulatilaka, J. Gord, Theoretical modeling of single-laser-  
23 shot, chirped-probe-pulse femtosecond coherent anti-Stokes Raman scattering thermometry.  
24 Appl. Phys. B 104 (2011) 699-714.

25  
26 [21] V. Moureau, P. Domingo, L. Vervisch, Design of a massively parallel CFD code for complex  
27 geometries. Comptes Rendus Mécanique 339 (2-3) (2011) 141–148.

28  
29 [22] M. Germano, U. Piomelli, P. Moin, W.H. Cabot, A dynamic subgrid-scale eddy viscosity  
30 model. Physics of Fluids A: Fluid Dynamics 3 (1991) 1760–1765.

31  
32 [23] P. Domingo, L. Vervisch, S. Payet, R. Hauguel, DNS of a premixed turbulent V-flame and  
33 LES of a ducted flame using a FSD-PDF subgrid scale closure with FPI-tabulated chemistry.  
34 Combust. Flame 143 (2005) 566–586.

35  
36 [24] J. Luche, M. Reuillon, J.C. Boettner, M. Cathonnet, Reduction of large detailed kinetic  
37 mechanisms: Application to kerosene/air combustion. Combustion Science and Technology,  
38 176(11) (2004) 1935–1963.

39  
40 [25] B. Abramzon, W.A. Sirignano, Droplet vaporization model for spray combustion  
41 calculations. Int. J. Heat Mass Transf. 32 (1989) 1605–1618.

42  
43 [26] P. Rosin, E. Rammler, The law governing the fineness of powdered coal. J. Inst. Fuel 7,  
44 (1933) 29–36.

45  
46  
47  
48  
49  
50  
51  
52  
53  
54  
55  
56  
57  
58  
59  
60  
61  
62  
63  
64  
65

1 [27] P. Domingo-Alvarez, P. Bénard, V. Moureau, F. Grisch, G. Lartigue, Impact of Spray Droplet  
2 Distribution on the Performances of a Kerosene Lean/Premixed Injector. *Flow, Turbulence and*  
3 *Combustion*, Springer Verlag (Germany), 104 (2020) 421-450.  
4  
5

6 [28] W. Meier, I. Boxx, M. Stöhr, C.D. Carter, Laser-based investigations in gas turbine model  
7 combustors, *Exp. Fluids*. 49 (2010) 865–882  
8  
9

10 [29] J. Samarasinghe, S.J. Peluso, B.D. Quay, D. a Santavicca, The three-dimensional structure  
11 of swirl-stabilized flames in a lean premixed multi-nozzle can combustor, in: *Proc. ASME Turbo*  
12 *Expo 2015 Turbine Tech. Conf. Expo. GT2015-42167* (2015).  
13  
14  
15

16 [30] D.G. Nicol, R.C. Steele, N.M. Marinov, P.C. Malte, The Importance of the Nitrous Oxide  
17 Pathway to NO<sub>x</sub> in Lean-Premixed Combustion, *Journal of Engineering for Gas Turbines and*  
18 *Power* 117 (1995) 100-112.  
19  
20  
21  
22  
23  
24  
25  
26  
27  
28  
29  
30  
31  
32  
33  
34  
35  
36  
37  
38  
39  
40  
41  
42  
43  
44  
45  
46  
47  
48  
49  
50  
51  
52  
53  
54  
55  
56  
57  
58  
59  
60  
61  
62  
63  
64  
65